Eur. J. Mineral., 35, 715–735, 2023
https://doi.org/10.5194/ejm-35-715-2023

European Journal of Mineralogy
Open Access

Partial melting of amphibole–clinozoisite eclogite at the pressure maximum (eclogite type locality, Eastern Alps, Austria)

Simon Schorn[1], **Anna Rogowitz**[1,2], **and Christoph A. Hauzenberger**[1]

[1]Institute of Earth Sciences, NAWI Graz Geocenter, University of Graz, Universitätsplatz 2, 8010 Graz, Austria
[2]Department of Geology, University of Vienna, Josef Holaubek-Platz 2, 1090 Vienna, Austria

Correspondence: Simon Schorn (simon.schorn@uni-graz.at)

Received: 16 April 2023 – Revised: 28 June 2023 – Accepted: 29 July 2023 – Published: 4 September 2023

Abstract. Pristine amphibole–clinozoisite eclogite from within the eclogite type locality (Hohl, Koralpe) of the Eastern Alps in Austria preserves centimetre-thick, concordant, laterally continuous leucocratic segregations of coarse-grained (up to $\sim$1 cm grain diameter) euhedral amphibole–clinozoisite–quartz and disseminated garnet–omphacite–rutile. The segregations locally show selvedges dominated by coarse-grained amphibole at the interface with their host eclogite. Retrogression is limited to thin films of texturally late plagioclase $\pm$ amphibole and minor symplectites of diopside–plagioclase partially replacing omphacite. Mineral compositions are largely homogeneous except for clinozoisite, which is significantly enriched in Fe^{3+}, rare-earth and high-field-strength elements in the rock matrix compared to that in segregations. Petrography, mineral chemical data and phase diagram modelling are interpreted in terms of limited melting under high-a_{H_2O} conditions, at or close to the well-established pressure maximum (21 ± 3 kbar and 680–740 °C), followed by melt crystallization near these conditions. Exsolution of melt-dissolved H_2O led to the formation of the amphibole-rich selvedges at the leucosome–eclogite interface. Plagioclase $\pm$ amphibole/clinopyroxene films formed at lower pressure from final melt vestiges adhering to grain boundaries or from secondary fluid–rock interaction. Natural variability in rock composition and the bulk oxidation state leads to variable mineral modes and calculated high-pressure solidus temperatures for compositional end-members sampled at Hohl. Modelling suggests that oxidized conditions ($X Fe^{3+} < 0.5$) favour hydrated but refractory amphibole–clinozoisite-rich assemblages with a fluid-present solidus temperature of $\sim$740 °C at 20 kbar, whereas more reduced conditions ($X Fe^{3+} \sim 0.2$) yield "true" eclogites (> 80 vol % garnet + omphacite) that commence melting at $\sim$720 °C at the same pressure. The interlayering of such eclogites potentially constitutes a fluid source–sink couple under appropriate pressure–temperature conditions, favouring fluid transfer from neighbouring dehydrating layers to melt-bearing ones down gradients in the chemical potential of H_2O (μH_2O). Phase diagram calculations show that for moderate degrees of fluid-fluxed melting ($\leq$ 10 vol % melt) near the pressure maximum, the observed equilibrium assemblage is preserved, provided the melt is subsequently removed from the source rock. The resulting hydrous melts may be, in part, parents to similar eclogite-hosted pegmatitic segregations described in the eclogite type locality. We suggest that eclogites with a comparable composition and metamorphic history are however unlikely to produce voluminous melts.

Published by Copernicus Publications on behalf of the European mineralogical societies DMG, SEM, SIMP & SFMC.

1 Introduction

Eclogites ($\geq 75\,\%$ garnet + omphacite; Carswell, 1990) are inherently rather refractory rocks because they contain subordinate quantities of hydrous minerals, depending on composition and the specific pressure–temperature evolution. Partial melting of eclogite therefore typically involves the breakdown of hydrous epidote-group minerals (Cao et al., 2018, 2020), phengite and/or amphibole (e.g. Schmidt et al., 2004; Cao et al., 2021), but nominally anhydrous minerals such as omphacite may also contribute (Feng et al., 2021). The solidus temperature in the basalt + water system increases with pressure (e.g. Schmidt and Poli, 2014); therefore most (ultra)high-pressure ((U)HP) eclogites attain peak pressure under subsolidus conditions (e.g. Wang et al., 2014; Cao et al., 2018). Melting commonly occurs at lower pressure during subsequent exhumation if and when the solidus is crossed during uplift (e.g. Deng et al., 2018). On the other hand, if water fluxing occurs, even relatively dry eclogites may experience variable degrees of melting (Schorn et al., 2021) due to the preferential consumption of clinopyroxene and H_2O (Laurie and Stevens, 2012). Regardless of the specific melting mechanisms, high-pressure melts are particularly H_2O-rich (e.g. Hermann et al., 2006). In cases where pressures were extreme, as reported in the Sulu belt in China (35 to > 55 kbar and > 850 °C; e.g. Xia et al., 2018), a complete evolution from solute-rich supercritical fluid to hydrous melt is proposed (Wang et al., 2020). If the melts sufficiently accumulate in order to segregate from their source and ascend through the lithosphere, it is suggested that they facilitate exhumation and contribute to crustal differentiation and growth in collisional settings (Labrousse et al., 2011). In particular, melting of eclogite in subduction zones is considered a source for hydrous arc magmas (e.g. Hernández-Uribe et al., 2020; Turner and Langmuir, 2022). When they pond in melt-dominated pockets, the high H_2O content prevents the melts from solidifying during exhumation and decompression, keeping the system melt-bearing until much lower pressures and temperatures are reached. Crystallized melt pockets are in fact commonly dominated by plagioclase and related to retrogression of the surrounding eclogite (e.g. Cao et al., 2018; Wang et al., 2014). This indicates solidification in the middle to upper crust, whereas reports of melt solidification at high-pressure eclogite-facies conditions (i.e. beyond the albite = jadeite + quartz transition) are rare. The conditions and processes related to high-pressure melting and melt solidification are therefore still controversial. We add to this discussion by reporting melting in a well-known eclogite occurrence located in the eclogite type locality of the Austrian Alps. Using petrographic observations, major- and trace-element mineral composition data, and thermodynamic modelling, we suggest that the studied amphibole–clinozoisite eclogites experienced low degrees of melting, leucosome formation and melt crystallization close to the pressure maximum recorded by these rocks. By modelling the effects of variable bulk compositions, we demonstrate that neighbouring eclogite layers may form a fluid source–sink couple due to contrasting solidus temperatures controlled by the natural compositional variability.

We use the term "melt" for mechanically separable silicate-rich liquid, while "fluid" refers to a distinct aqueous fluid (commonly called "water", particularly in the experimental literature). "H_2O" refers to the chemical component, regardless of whether it is bound as OH groups in hydrous minerals or dissolved in fluid or melt. In thermodynamic modelling, aqueous fluid is commonly approximated with pure H_2O; in this case it simultaneously describes the chemical component and the fluid phase. To emphasize this difference we refer to such a pure H_2O fluid as "free H_2O". $M(H_2O)$ refers to the total molar amount of H_2O present as a component in the chemical system under consideration.

2 Geological setting

The eclogite occurrences of the Koralpe and Saualpe of the polymetamorphic Austroalpine basement (south-eastern Austria, Fig. 1a) constitute the type locality of eclogite (Haüy, 1822). Eclogites and metagabbros occur as numerous metre- to kilometre-sized lenses within retrogressed paragneisses (Pilger and Schönenberg, 1975; Weissenbach et al., 1978). The eclogite-facies unit is structurally overlain by greenschist- to amphibolite-facies metasediments, quartzites and marbles (Fig. 1b; e.g. Kleinschmidt, 1974; Gregurek et al., 1997). Normal-MORB-type gabbros and basalts (e.g. Miller et al., 1988) intruded the thinned Tethyan passive margin in Permian times at 275 ± 18 Ma (Thöni and Jagoutz, 1992). The subsequent collision of Europe and the Adriatic plate led to widespread "Eoalpine" high-pressure metamorphism in the Cretaceous at ca. 90 Ma (Thöni and Jagoutz, 1992). The trace of this subduction zone extends for about 400 km from the Texel Complex in the west to the Pohorje Complex in the east (Fig. 1a; Thöni and Jagoutz, 1993). Eoalpine pressure–temperature (P–T) conditions increase from west to east, reaching diamond-grade UHP conditions of > 35 kbar and 800–850 °C in the Pohorje Mountains (Janák et al., 2015). Reported pressure maxima and metamorphic ages for the Koralpe–Saualpe eclogites are 18–20 kbar and 600–650 °C at 100 ± 10 Ma (Miller and Thöni, 1997); 22 ± 2 kbar and 630–740 °C at 91.1 ± 1.3 Ma (Thöni et al., 2008); and 16.5–20.5 kbar and 620–720 °C (Bruand et al., 2010), ∼ 23–24 kbar and 640–690 °C (Schorn and Stüwe, 2016), 21 ± 2 kbar and 700 ± 20 °C (Schorn et al., 2021), and 22–25 kbar and 670–700 °C at 101 ± 1.2 to 92.6 ± 2 Ma (Miladinova et al., 2022). Phengitic cores in white mica of coexisting paragneisses yield similar conditions of 20 kbar and 680 °C between 90.9 ± 0.7 and 88.5 ± 1.7 Ma (Sm–Nd garnet–whole-rock isochron age; Thöni and Miller, 1996). The eclogite-facies units were partly exhumed along the Plattengneiss shear

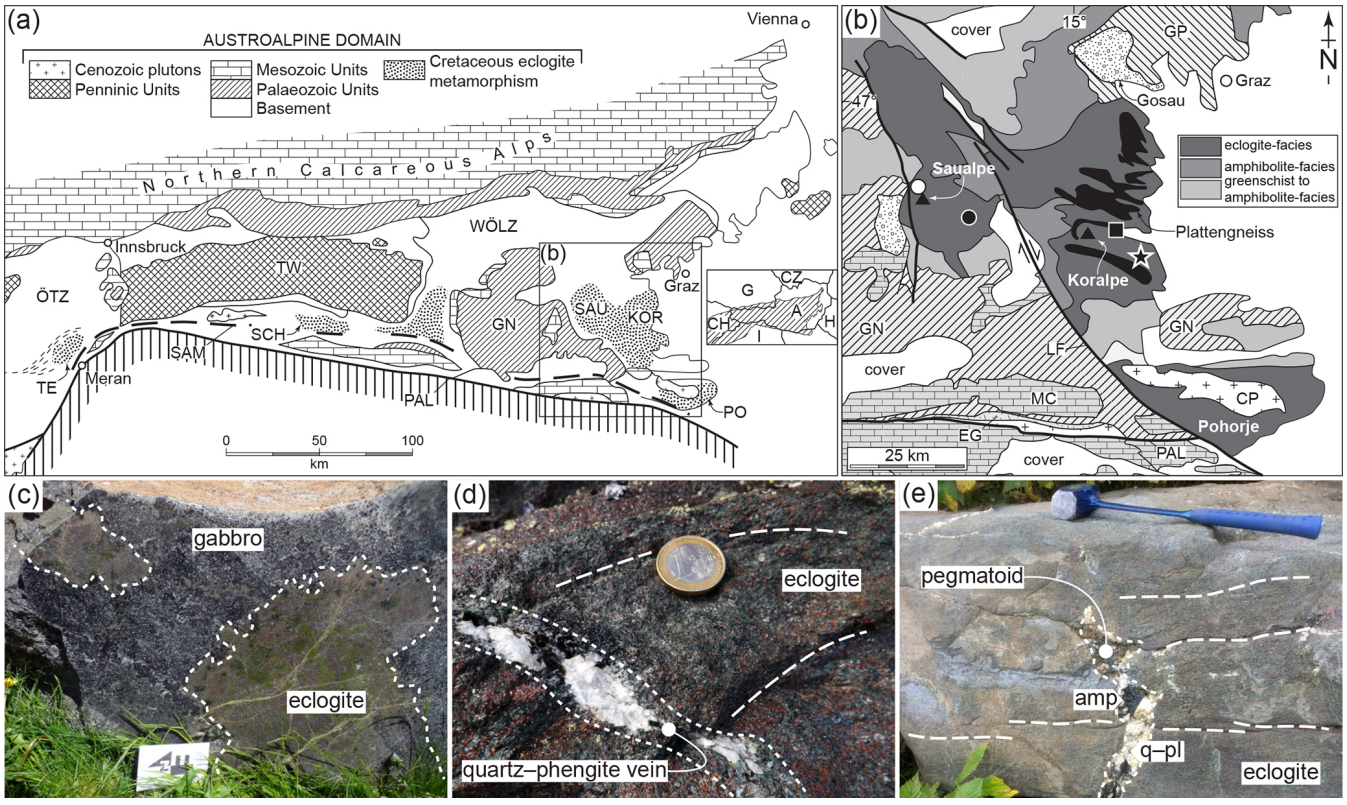

Figure 1. (a, b) Geological outline (after Schorn et al., 2021). **(a)** Simplified tectonic map of the Eastern Alps (after Schmidt et al., 2004; Thöni et al., 2008) with the main structures and domains: Ötztal–Stubai Complex (Ötz), Tauern Window (TW), Wölz nappe system (WÖLZ), Gurktal nappe system (GN) and Periadriatic lineament (PAL). Cretaceous eclogite-facies units are highlighted by dotting: Texel (TE), Schober (SCH), Saualpe (SAU), Koralpe (KOR) and Pohorje Complex (PO). The rectangle corresponds to **(b)**. **(b)** Simplified geological map showing the metamorphic grade and main units of the Saualpe and Koralpe area (after Froitzheim et al., 2008; Thöni et al., 2008): Gosau sediments, Graz Palaeozoic (GP), Cenozoic plutons (CP), Eisenkappel granite (EG), Mesozoic Austroalpine cover (MC), Lavanttal fault (LF), and Cenozoic and Plio-/Pleistocene cover (CPC). The approximate position of the Plattengneiss shear zone is given in black (modified after Putz et al., 2006). The star marks the sampling locality (46°43′49.0″ N, 15°08′45.9″ E). The black square gives the location of partially eclogitized gabbro (shown in **c**; Schorn and Diener, 2017, photo credit: Kurt Stüwe). The black dot indicates the location of high-pressure veins shown in **(d)** and fluid-fluxed melting of eclogite (shown in **e**; Schorn et al., 2021). The white dot gives the locality of Eoalpine-aged metapelite melting (Thöni and Miller, 2010) in the Saualpe area. **(c–e)** Key outcrop photographs. White lines with long dashes highlight the high-pressure fabric. Abbreviations: amp, amphibole; pl, plagioclase; q, quartz. The coin is ∼ 2.3 cm in diameter; the hammer is ∼ 40 cm long.

zone, a flat-lying metapelitic mylonite of up to 600 m in thickness (Fig. 1b; Putz et al., 2006; Schorn and Stüwe, 2016). Prior to tectonic dismemberment along the Lavanttal fault in the Early Miocene (Fig. 1b; Kurz et al., 2011), the basements of the Koralpe–Saualpe formed a coherent block with a shared tectonometamorphic history.

2.1 Eoalpine fluid–rock interaction and anatexis

Eclogitization of the mafic protoliths is documented along a locally preserved reaction front (Fig. 1c; Schorn and Diener, 2017), suggested to be triggered by fluid released from the pelitic host rock at high pressure (Schorn, 2018). Locally high a_{H_2O} and fluid infiltration under eclogite-facies conditions are inferred from discordant quartz–phengite veins (Fig. 1d; Miller, 1990). Phase diagram modelling of representative metapelite and eclogite using a fixed $M(H_2O)$ predicts that at high pressure, the solid assemblages coexist with minor free H_2O (dotted region in Fig. 2), bound by the solidus towards high temperature. At lower pressure the rocks are H_2O-absent, causing the solidus to shift towards higher temperature. The mineral-bound H_2O in the metapelite allows for dehydration after exhumation to mid-crustal conditions (Fig. 2), where the rocks have pervasively retrogressed (Schorn, 2018; Schorn et al., 2021). The eclogite is expected to remain H_2O-absent during decompression, favouring the preservation of high-P assemblages in the absence of externally sourced fluid infiltration (Fig. 2; Schorn et al., 2021).

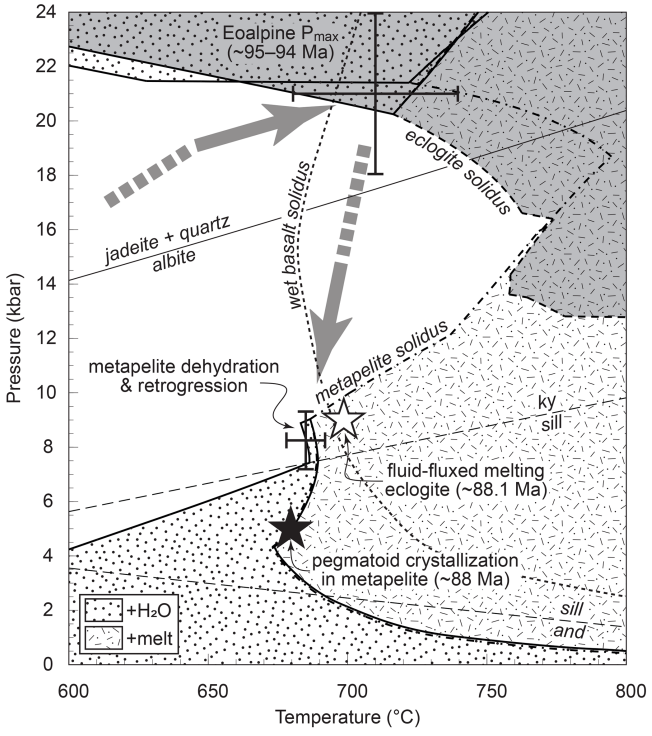

Figure 2. Summary of pressure–temperature evolution of the eclogite type locality during the Eoalpine cycle. References for P_{max} conditions are given in the text. Calculated eclogite and metapelite phase assemblage fields, retrogression conditions, and fluid-fluxed melting of eclogite (white star) are from Schorn et al. (2021) assuming a fixed $M(H_2O)$. Grey shading marks fields for eclogite. The black star is for pegmatoid crystallization in metapelite (Thöni and Miller, 2010). The dotted line is the water-present basalt solidus for reference (Schmidt and Poli, 1998). The arrow is a generic Eoalpine P–T loop. Abbreviations: and, andalusite; ky, kyanite; sill, sillimanite.

Whereas the pressure–temperature evolution during the Eoalpine cycle lies close to the solidus (Fig. 2), evidence for partial melting is rarely preserved and is restricted to localized pegmatitic segregations in metapelite (Fig. 1b; Thöni and Miller, 2010) and eclogite ("pegmatoid" in Fig. 1e; Heede, 1997; Schorn et al., 2021) in the Saualpe basement. In both cases melting was fluid-assisted; postdates the timing of Eoalpine P_{max} (ca. 88 Ma; Heede, 1997; Thöni and Miller, 2010); and occurred at mid-crustal depths during late-stage exhumation, under or near the conditions of metapelite dehydration (Fig. 2; Schorn et al., 2021). We present petrographic data and pseudosection modelling of amphibole–clinozoisite eclogite sampled at a well-studied locality of the Koralpe (the "Hohl eclogite"; e.g. Bruand et al., 2010; Miladinova et al., 2022) to show that previously unreported partial melting and melt crystallization occurred in a relatively narrow P–T window close to the Eoalpine pressure maximum.

2.2 Hohl

The Hohl eclogite consists of partly eclogitized metagabbro and well-equilibrated amphibole–clinozoisite ± kyanite eclogite (e.g. Miller et al., 1988; Bruand et al., 2010; Miladinova et al., 2022). The investigated samples belong to the latter group and are characterized by a granoblastic texture and a pervasive, NE-dipping foliation (N030/40). The main fabric-forming minerals are omphacite, clinozoisite and amphibole (hornblende; see below), all found as stubby to elongated crystals of similar size distribution, typically around 2–4 mm in length. Garnet is finer-grained (≤ 1 mm) but occasionally reaches up to ∼ 5 mm in diameter. The matrix is disrupted by roughly foliation-parallel leucocratic segregations with variable thicknesses along strike (∼ 1–4 cm; Fig. 3a). The segregations can be traced over several metres and are termed "leucosome". The leucosomes are heterogeneously spaced and occur about every 10–50 cm within the rock (Figs. 3 and 4). Locally, they form veins in the neck of foliation boudinages (Fig. 3b, c). The leucosomes consist of pale-yellow euhedral blades of clinozoisite (up to 2 cm in length; ∼ 20 vol %–40 vol %), coarse-grained (max ∼ 1 cm) subhedral-to-euhedral black amphibole (∼ 20 vol %–30 vol %) and anhedral variably sized quartz (up to ∼ 50 vol %; Fig. 3c, d). Garnet and omphacite with similar grain size and shape to the matrix minerals are disseminated within the structures. Locally, the leucosomes are decorated by amphibole-rich selvedges at the rims (Fig. 4).

3 Methods

3.1 Petrography

Rock specimens were sampled over several field trips with the first numbers referring to the sampling year. Thin sections were analysed using a standard petrographic microscope. Mineral proportions were estimated on thin-section scans and with image analysis software (∼ 10 %–20 % uncertainty due to grain size distribution) based on colour contrast between minerals.

3.2 Major-element mineral composition

Backscattered electron (BSE) images and mineral compositions were acquired using a JEOL JXA-8530FPlus HyperProbe electron probe microanalyser (EPMA) equipped with an energy-dispersive (ED) and five wavelength-dispersive (WD) spectrometers housed at the Institute of Earth Sciences, NAWI Graz Geocenter, University of Graz. Measurement conditions were 15 kV accelerating voltage, 10 nA beam current and a beam diameter of 1–5 µm depending on the analysed mineral. A range of synthetic and natural mineral standards were used for element calibration. Selected analyses were carried out using a Cameca SX Five EPMA lo-

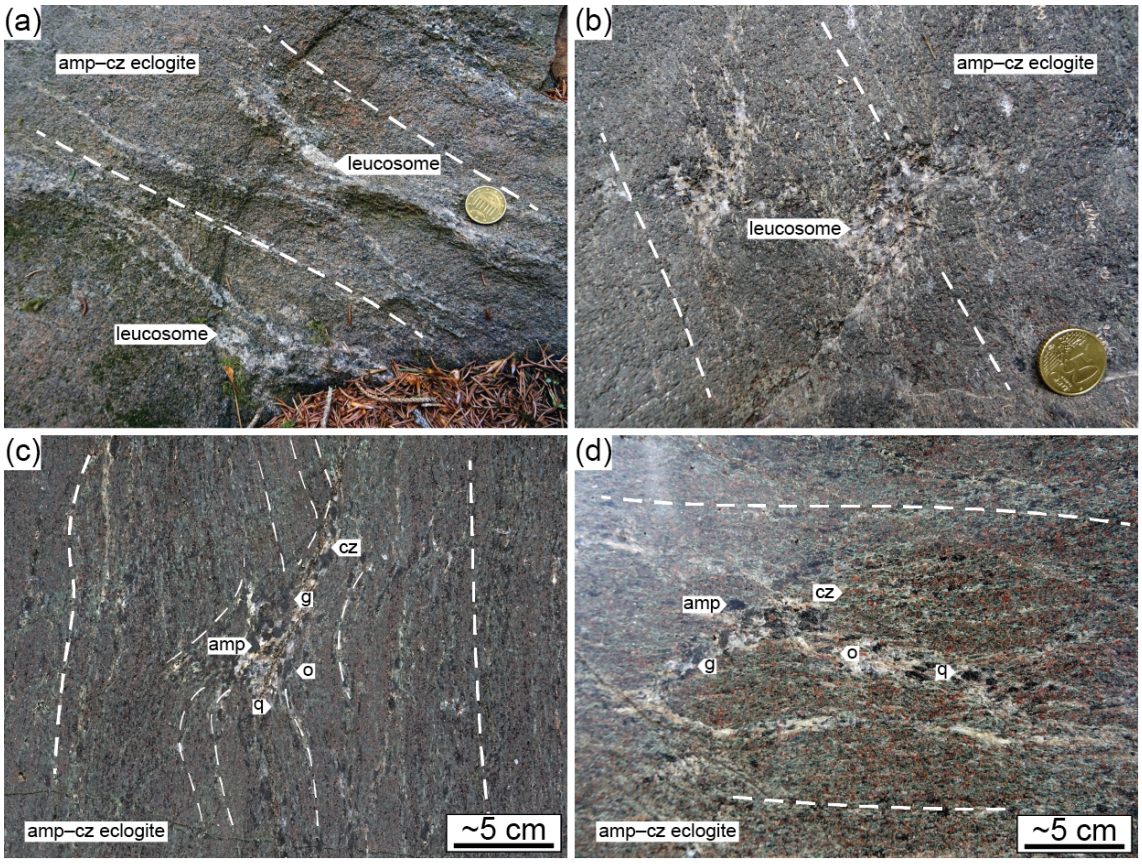

Figure 3. Outcrop photographs **(a, b)** and polished boulders **(c, d)** of leucosome-bearing amphibole–clinozoisite eclogites at Hohl. Dashed white lines indicate foliation traces. The coin diameter is ∼ 2.5 cm. Abbreviations: cz, clinozoisite; g, garnet; o, omphacite.

cated at the Department of Lithospheric Research, University of Vienna. Measurement conditions were 15 kV accelerating voltage and 20 nA beam current. Mineral formulae were calculated with PET7 (Dachs, 1998) using the method of Droop (1987) for Fe^{3+} determination. For clinozoisite and plagioclase analyses, total iron is given as Fe_2O_3. Representative mineral chemical data are summarized in Table 1. Additional analyses are reported in the Supplement, Table S1.

3.3 Trace-element and rare-earth-element mineral composition

Laser ablation–inductively coupled plasma–mass spectrometry (LA–ICP–MS) was used for determining the trace-element and rare-earth-element composition of selected minerals. Measurements were made using an Agilent 7500cx and 7900 quadrupole ICP–MS system (Central Lab Water, Minerals and Rocks, NAWI Graz Geocenter, University of Graz and Graz University of Technology) coupled to an Elemental Scientific 193 nm excimer laser with a spot size of 50 µm and 0.8 L He flow rate. The laser was operated at an 8 Hz repetition rate, and the fluence was set to $\sim 4\,J\,cm^{-2}$. The USGS reference glass BCR-2G (Rocholl, 1998) was measured for quality control; data were reproduced within 10 % error. Data for all elements were reduced using the NIST SRM 612 (Jochum et al., 2011) standard. Silicon was used as the internal calibrant. The software GLITTER 4.0 (Griffin, 2008) was used for data reduction. Rare-earth-element (REE) data were normalized with respect to chondrite (Boynton, 1984) and plotted using the R-based software package GCDkit (Janoušek et al., 2006). Analyses are presented in the Supplement, Table S2.

3.4 Whole-rock element composition

Whole-rock chemical compositions were determined by X-ray fluorescence (XRF). A total of 1 g per sample was mixed with 7 g of lithium tetra-/metaborate; fused at ∼ 1300 °C to produce a glass disc; and analysed using a Bruker S8 TIGER XRF instrument located at the Institute of Earth Sciences, NAWI Graz Geocenter, University of Graz. About 100 international reference samples were used for calibration, and reference materials GSP-2 and OU-7 were analysed routinely as a precision monitor. Whole-rock data and the model composition are given in Table 2.

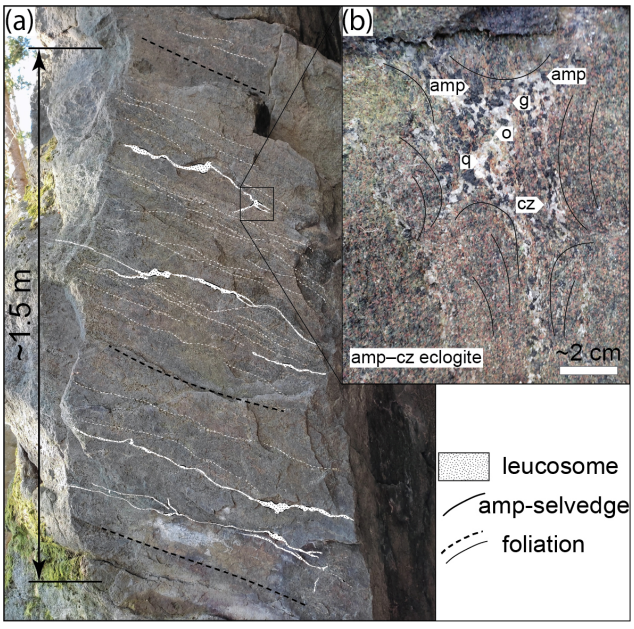

Figure 4. (a) Texture of leucosome-bearing eclogite cliff. Thick segregations locally show amphibole-rich selvedges. Dashed white lines indicate thin leucosomes. **(b)** Detail of veins surrounded by collapsed foliation.

Phase equilibrium modelling

Phase diagrams were calculated using THERMOCALC v3.47 (Powell and Holland, 1988) and an updated version of the Holland and Powell (2011) dataset (file tc-ds633.txt, created 23 June 2017). The activity–composition models used are diopside–omphacite–jadeite, clinoamphibole and tonalitic melt of Green et al. (2016); silicate-bearing aqueous fluid of Holland et al. (2018); muscovite–paragonite and ilmenite–hematite of White et al. (2014a); garnet of White et al. (2014b); and clinozoisite–epidote of Holland and Powell (2011). The aluminosilicates, paragonite (in Fig. 10), quartz, rutile, zoisite and H_2O are pure end-member phases. Phase abbreviations, except for amphibole (amp), are those used by THERMOCALC: albite (ab), andalusite (and), clinozoisite (cz), silicate-bearing aqueous fluid (fl), garnet (g), hematite (hem), hornblende (hb), pure aqueous fluid (H_2O), kyanite (ky), muscovite (mu), omphacite (o), paragonite (pa), quartz (q), rutile (ru), sillimanite (sill), tonalitic melt (L) and zoisite (zo). Phase proportion plots ("modeboxes") were constructed using unpublished Mathematica scripts (Roger Powell, personal communications, 2017), where phase abundances were calculated as mole fractions, with each phase normalized to one oxide sum total to approximate volume percent.

4 Petrography

4.1 Eclogite matrix

The matrix of all investigated samples consists of amphibole–clinozoisite–garnet–omphacite–rutile–quartz in variable proportions (Fig. 5). "True" eclogites (garnet + omphacite: ∼ 80 vol %; amphibole: ∼ 10 vol %; clinozoisite: ∼ 5 vol %; e.g. HO22-2, Fig. 5a, left) and amphibole–clinozoisite-rich varieties (garnet + omphacite: ∼ 50 vol %; amphibole: ∼ 30 vol %; clinozoisite: ∼ 15 vol %; e.g. HO21-1b, Fig. 5a, right) bracket the modal spread at Hohl, with the other samples (HO21-1a, HO21-5, HO22-8, HO23-1F; Fig. S1) falling within this range. All samples contain quartz (∼ 5 vol %–10 vol %) and rutile (∼ 1 vol %), forming interstitial grains and inclusions (Fig. 6a). Apatite, zircon and pyrite are accessory minerals. Grains mostly share sharp grain boundaries (Figs. 5a and 6a, b), and elongated grains such as omphacite, clinozoisite and amphibole define a planar fabric (Fig. 5a). Garnet forms subhedral grains ranging between < 0.5 and ∼ 5 mm in size (Figs. 5a and 6a, b). Larger garnets are predominantly rounded and contain abundant inclusions at the cores, mostly of fine-grained quartz and rutile (Fig. 5a) but also of subhedral crystals of amphibole and omphacite (Fig. 6a). Small garnets form slightly elongated grains and are free of inclusions or host minute quartz grains and rutile needles throughout the grain. Omphacite is found as pale-green elongated laths ranging between ∼ 2–4 mm in length (Fig. 5a). Grains are poor in inclusions but may host fine-grained garnet, amphibole, quartz and rutile (Fig. 6a, b). Omphacite grains show limited retrogression to diopside–plagioclase symplectites at rims. Amphibole occurs as stubby-to-elongated, olive-green–brown-green, pleochroic, anhedral laths, typically about 1–3 mm in length (Figs. 5a and 6a, b). Larger grains are poikilitic and include fine-grained garnet, clinozoisite, rutile and quartz. Clinozoisite forms thin colourless needles that are typically ∼ 1–2 mm in length and may include minute grains of rutile and/or quartz (Figs. 5a and 6a, b).

4.2 Leucocratic segregations

The segregations are best developed in amphibole–clinozoisite-rich eclogites (e.g. HO23-1F; Fig. 5b), while garnet–omphacite-dominated rocks (e.g. HO22-2; Fig. 5a, left) lack distinct leucosomes. The segregations host the identical matrix mineral assemblage but differ in terms of modal abundance and grain size (Figs. 5b and 6c, d). They are dominated by coarse-grained (∼ 1–3 mm) anhedral quartz and large (up to ∼ 2 cm) euhedral blades of clinozoisite (Figs. 5b and 6c, d). Amphibole is abundant and forms subhedral-to-euhedral grains, in particular within and next to quartz–clinozoisite layers (Fig. 5b). In selvedges bounding the leucosomes, it is significantly more coarsely grained (up to ∼ 5 mm) than in the nearby matrix and contains numer-

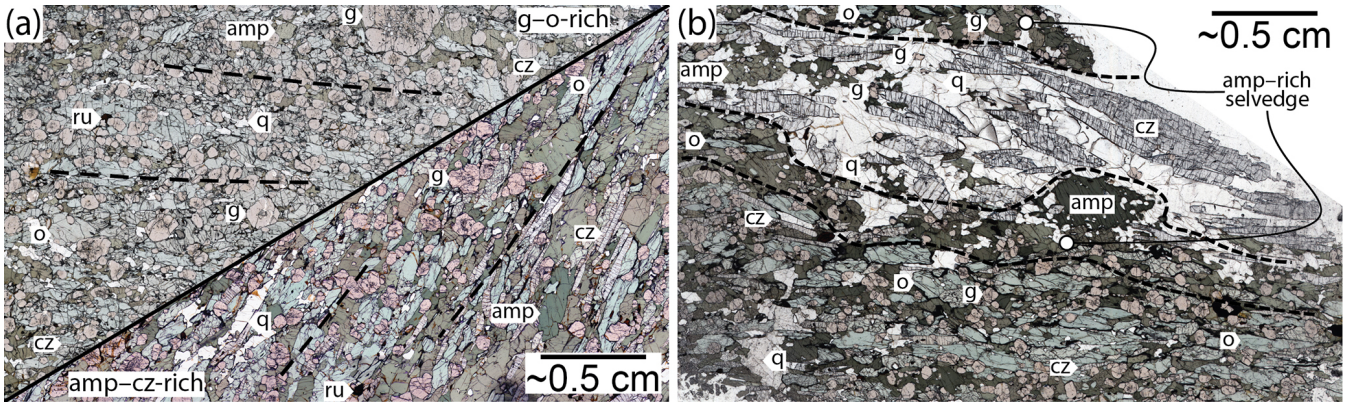

Figure 5. Thin-section scans. **(a)** Matrix. Left: garnet–omphacite-rich sample (HO22-2). Cores of large garnets (max 5 mm; e.g. centre north) are clouded with inclusions. Right: amphibole–clinozoisite-rich sample (HO21-1b). Note the preferred mineral orientation defining the metamorphic foliation (dashed lines). **(b)** Segregation and surroundings in amphibole–clinozoisite-rich sample (HO23-1F). Clinozoisite forms euhedral blades of up to ∼ 1.5 cm in length. Note the abundance of amphibole at the borders of clinozoisite–quartz-rich area. Thin sections in (**a**, right) and **(b)** are slightly thick, thus enhancing the colours. Abbreviation: ru, rutile.

ous inclusions (Fig. 5b). Plagioclase forms symplectites and thin films next to amphibole, commonly doubling former grain boundaries together with a thin layer of Na-rich diopside and/or amphibole found away from the large amphibole ("amp II" in Fig. 6c, d). Plagioclase typically separates amphibole from quartz and clinozoisite and may occupy triple junctions where these minerals form acute angles (Fig. 5h). This texture occurs particularly in segregations and within adjacent amphibole-rich selvedges (Fig. 6e–g). The films are mostly discontinuous but locally envelop entire grains. They are never observed in contact with omphacite or related diopside–plagioclase symplectites. Similar films occur in eclogite-hosted pegmatoids (Fig. 1e; Schorn et al., 2021), where they occur in the same textural location. Omphacite, garnet and rutile grains are disseminated throughout the leucosomes (Figs. 5b and 6c, d), with the latter showing comparable size and shape to grains in the rock matrix. Omphacite grains are slightly enlarged compared to the matrix mineral and locally display thin diopside–plagioclase symplectites at the rims (Figs. 5b and 6c).

5 Mineral chemistry

5.1 Major elements

All analysed minerals display limited variability in terms of major-element composition (Tables 1 and S1). Site fractions are in atoms per formula unit (a.p.f.u.), whereas their ratios are dimensionless if not specified otherwise. Garnet is generally rich in almandine (cores: 0.44–0.50; rims: 0.45–0.48), followed by pyrope (cores: 0.23–0.30; rims: 0.25–0.31) and similar grossular contents (cores: 0.23–0.28; rims: 0.22–0.26). Spessartine is low (0.01–0.02). Garnet in garnet–omphacite-rich samples (e.g. HO22-2; Fig. 5a, left) shows a slightly larger variability in X_{Fe} ($= \frac{Fe}{Fe+Mg}$) of 0.62–0.68 and an average of ∼ 0.64 (Tables 1 and S1) compared to amphibole–clinozoisite-rich ones (e.g. HO21-1b – Fig. 5a, right; HO23-1F – Fig. 5b) with a slightly lower X_{Fe} of 0.60–0.63 and an average of ∼ 0.62.

Omphacite is Na-rich, with a j(cpx) ($= \frac{Na}{Na+Ca}$) of 0.38–0.42, and Fe-poor with a somewhat variable X_{Fe} of 0.06–0.20. Inclusions in garnet and omphacite in true eclogite samples show a slightly higher X_{Fe} of 0.16 on average and j(cpx) of 0.40, whereas omphacite in segregations and cores of larger grains has values of ∼ 0.10 and 0.41, respectively. Fe^{3+} is calculated between 0.02–0.14; cores are slightly enriched with ∼ 0.10 on average, while rims and omphacite in true eclogite samples have values of ∼ 0.06–0.07. Clinopyroxene that forms thin rims on amphibole and symplectites on omphacite is a relatively Na-rich diopside with j(cpx) = 0.11 to 0.18 and variable X_{Fe} = 0.04 to 0.18. Potassium in clinopyroxene is negligible.

Amphibole is part of the calcic group following the nomenclature of Leake et al. (1997) and is called hornblende here. Inclusions in garnet are classified as aluminopargasite and are relatively Fe- and Al-rich, with X_{Fe} = 0.38 to 0.44 and Al^{VI} = 1.15 to 1.45, respectively. Amphibole in the rock matrix, leucosomes, selvedges and included in omphacite is edenite–aluminoedenite and compositionally homogeneous, with X_{Fe} = 0.27 to 0.33 and Al^{VI} = 0.73 to 1.00. No clear compositional trend among samples and textural locations is evident. Amphibole that forms thin rims on large grains has an X_{Fe} of 0.25–0.30 and Al^{VI} of 0.47–0.51. Fluorine, Cl and calculated Fe^{3+} are negligible in all cases.

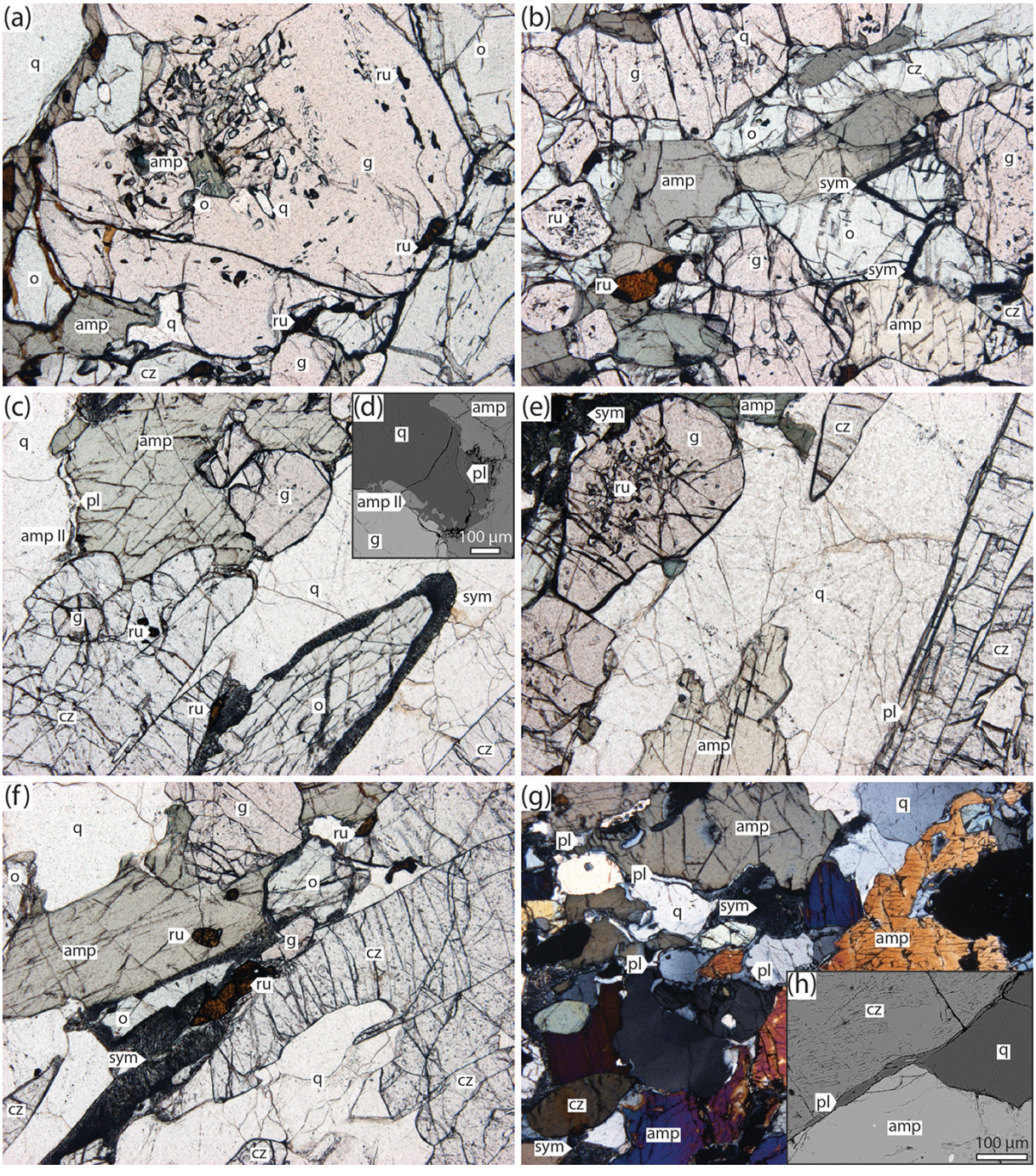

Figure 6. Microphotographs of investigated amphibole–clinozoisite eclogites. Panels **(a)** and **(b)** show the rock matrix, panels **(c)**–**(f)** are segregations, and panel **(g)** shows the matrix next to segregations. **(a)** Large (∼ 3 mm) poikilitic garnet-hosting inclusions of amphibole, omphacite, rutile and quartz (HO22-2). **(b)** Equigranular matrix showing sharp grain boundaries between garnet–omphacite–amphibole–clinozoisite–rutile (HO21-1b). Locally omphacite displays minor retrogression by fine-grained symplectites of diopside–plagioclase (sym). **(c–f)** Coarse-grained (up to ∼ 5 mm) amphibole–clinozoisite–quartz coexisting with garnet, omphacite and rutile in segregation (HO22-8). Omphacite is locally retrogressed to symplectites. **(d)** BSE picture showing thin rims of texturally late amphibole (amp II) and plagioclase film between coarse-grained amphibole and quartz. **(g)** Amphibole-rich portion close to a segregation (HO23-1F). Thin plagioclase films are found preferentially between hornblende and quartz (crossed polars). **(h)** BSE picture of plagioclase film at an amphibole–clinozoisite–quartz triple junction. Omphacite shows variable decomposition to symplectites. The field of view is 4.5 mm in all microphotographs.

Table 1. Major-element mineral composition for representative samples.

Sample	HO22-8	HO22-2		HO23-1F		HO22-8	HO22-2	HO23-1F	HO22-2		HO22-8	HO23-1F				HO22-2		HO22-8			HO23-1F			HO22-8
Mineral		Garnet					Omphacite				Amphibole					Clinozoisite								Plagioclase
Position	core	core	rim	core	rim	core	rim	rim	mtx	mtx	lcs	mtx	lcs	slv	sym	mtx (core)	mtx (rim)	mtx (rim)	lcs (core)	lcs (rim)	mtx	lcs (core)	lcs (rim)	film
SiO_2	39.03	38.69	38.97	38.98	38.98	54.66	54.53	54.80	45.33	45.65	45.76	46.97	46.06	46.72	46.15	38.56	39.04	38.16	39.63	38.83	38.21	39.26	39.02	64.68
TiO_2	0.03	0.03	0.07	0.09	0.05	0.15	0.17	0.16	0.58	0.54	0.51	0.48	0.54	0.54	1.05	0.15	0.17	0.18	0.06	0.08	0.18	0.08	0.07	bd
Al_2O_3	21.69	21.60	21.73	21.75	21.91	10.08	10.56	9.60	16.08	15.94	13.37	13.79	13.43	13.39	10.46	28.75	28.92	28.68	31.61	31.57	28.72	31.74	31.72	21.83
Cr_2O_3	0.02	0.09	0.08	0.03	0.14	nd	nd	nd	nd	nd	nd	nd	nd	nd	nd	nd	nd	nd	nd	nd	nd	nd	nd	nd
FeO*	22.27	24.30	22.70	21.67	21.94	5.14	5.04	5.51	10.72	10.88	11.42	9.65	10.69	9.53	9.28	6.72	6.27	6.75	2.79	2.79	6.87	2.76	3.03	0.10
MnO	0.72	0.58	0.37	0.67	0.65	0.03	0.05	0.05	0.03	0.09	0.07	0.06	0.08	0.05	bd	0.03	0.03	bd	bd	bd	bd	bd	bd	bd
MgO	7.08	5.91	7.41	6.81	7.19	8.96	8.76	8.97	12.02	11.98	13.23	13.68	13.70	14.07	15.48	0.20	0.17	0.21	bd	bd	0.19	bd	0.04	bd
CaO	9.11	9.50	8.75	10.33	9.44	15.51	15.60	15.54	9.26	9.41	10.24	9.40	9.63	9.66	12.12	24.19	24.29	24.32	25.03	25.06	24.36	24.96	24.99	3.21
Na_2O	0.03	0.02	0.02	0.03	0.03	5.73	5.78	5.76	3.86	3.79	3.61	3.74	3.56	3.69	2.48	bd	bd	bd	bd	bd	bd	bd	0.02	9.99
K_2O	nd	nd	nd	nd	nd	bd	bd	bd	0.43	0.41	0.25	0.27	0.25	0.25	0.26	bd	bd	bd	bd	bd	bd	bd	bd	0.06
Cl	nd	nd	nd	nd	nd	bd	bd	bd	0.02	0.01	bd	0.02	0.02	bd	0.02	bd	bd	bd	bd	bd	bd	bd	bd	bd
Total	99.96	100.72	100.10	100.36	100.33	100.26	100.48	100.39	98.32	98.69	98.45	98.06	97.95	97.90	97.30	98.59	98.89	98.29	99.12	98.33	98.53	98.78	98.87	99.87
Oxygen	12	12	12	12	12	6	6	6	23	23	23	23	23	23	23	12.5	12.5	12.5	12.5	12.5	12.5	12.5	12.5	8
Si	3.00	2.97	2.99	2.98	2.98	1.95	1.94	1.96	6.48	6.51	6.58	6.69	6.62	6.67	6.69	2.98	3.00	2.96	3.00	2.97	2.95	2.98	2.97	2.86
Ti	0.00	0.00	0.00	0.01	0.00	0.00	0.01	0.00	0.06	0.06	0.06	0.05	0.06	0.06	0.11	0.01	0.01	0.01	0.00	0.01	0.01	0.01	0.00	0.00
Al	1.96	1.96	1.96	1.96	1.97	0.42	0.44	0.40	2.71	2.68	2.27	2.32	2.28	2.25	1.79	2.61	2.62	2.62	2.82	2.84	2.62	2.84	2.84	1.14
Cr	0.00	0.01	0.01	0.00	0.01	0.00	0.00	0.00	0.00	0.00	0.00	0.00	0.00	0.00	0.00	0.00	0.00	0.00	0.00	0.00	0.00	0.00	0.00	0.00
Fe^{3+}	0.05	0.09	0.06	0.08	0.06	0.06	0.06	0.08	0.00	0.00	0.00	0.00	0.00	0.00	0.00	0.39	0.36	0.39	0.16	0.16	0.40	0.16	0.17	0.00
Fe^{2+}	1.38	1.47	1.40	1.31	1.34	0.09	0.09	0.09	1.28	1.30	1.37	1.15	1.29	1.14	1.12	0.00	0.00	0.00	0.00	0.00	0.00	0.00	0.00	0.00
Mn	0.05	0.04	0.02	0.04	0.04	0.00	0.00	0.00	0.00	0.01	0.01	0.01	0.01	0.01	0.00	0.00	0.00	0.00	0.00	0.00	0.00	0.00	0.00	0.00
Mg	0.81	0.68	0.85	0.78	0.82	0.48	0.47	0.48	2.56	2.55	2.84	2.91	2.94	3.00	3.34	0.02	0.02	0.02	0.00	0.00	0.02	0.00	0.01	0.00
Ca	0.75	0.78	0.72	0.85	0.77	0.59	0.60	0.59	1.42	1.44	1.58	1.44	1.48	1.48	1.88	2.00	2.00	2.02	2.03	2.05	2.02	2.03	2.04	0.15
Na	0.00	0.00	0.00	0.00	0.00	0.40	0.40	0.40	1.07	1.05	1.01	1.03	0.99	1.02	0.70	0.00	0.00	0.00	0.00	0.00	0.00	0.00	0.00	0.86
K	0.00	0.00	0.00	0.00	0.00	0.00	0.00	0.00	0.08	0.08	0.05	0.05	0.05	0.05	0.05	0.00	0.00	0.00	0.00	0.00	0.00	0.00	0.00	0.00
Cl	0.00	0.00	0.00	0.00	0.00	0.00	0.00	0.00	0.01	0.00	0.00	0.01	0.01	0.00	0.01	0.00	0.00	0.00	0.00	0.00	0.00	0.00	0.00	0.00
Total	8.00	8.00	8.00	8.00	8.00	4.00	4.00	4.00	15.67	15.66	15.76	15.64	15.70	15.68	15.68	8.02	8.00	8.02	8.01	8.03	8.03	8.02	8.03	5.00
X_{Fe}	0.63	0.68	0.62	0.63	0.62	0.16	0.16	0.16	0.33	0.34	0.33	0.28	0.30	0.28	0.25	–	–	–	–	–	–	–	–	
X_{Alm}	0.46	0.50	0.47	0.44	0.45	–	–	–	–	–	–	–	–	–	–	–	–	–	–	–	–	–	–	
X_{Prp}	0.27	0.23	0.28	0.26	0.28	–	–	–	–	–	–	–	–	–	–	–	–	–	–	–	–	–	–	
X_{Grs}	0.25	0.26	0.24	0.28	0.26	–	–	–	–	–	–	–	–	–	–	–	–	–	–	–	–	–	–	
X_{Sps}	0.02	0.01	0.01	0.02	0.01	–	–	–	–	–	–	–	–	–	–	–	–	–	–	–	–	–	–	
j(cpx)	–	–	–	–	–	0.40	0.40	0.40	–	–	–	–	–	–	–	–	–	–	–	–	–	–	–	

* Fe_2O_3 for clinozoisite and plagioclase. Abbreviations: nd, not determined; bd, below detection limit; mtx, matrix; lcs, leucosome; slv, selvedge; sym, symplectite.

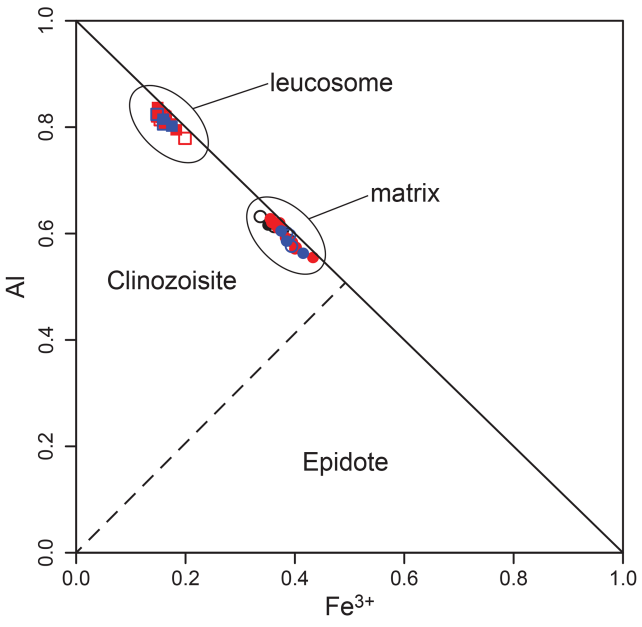

Figure 7. Binary M3-site Al–Fe^{3+} plot for clinozoisite data (Table S1). Al(M3) = $Al^{tot} - 2 - (3 - Si)$. Black: sample HO22-2; red: sample HO23-1F; blue: sample HO22-8. Filled symbols are for cores; empty ones are rims. Values are in atoms per formula unit.

Clinozoisite is a binary epidote–clinozoisite solid solution. The matrix mineral shows elevated Fe^{3+} (0.34–0.43) and intermediate M3-site Al (0.56–0.63), while the leucosome variety displays the opposite trend with an Fe^{3+} of 0.15–0.20 and M3-site Al of 0.78–0.84 (Fig. 7). Clinozoisite in the matrix of true eclogite samples shows a slightly lower Fe^{3+} of 0.36 on average.

Plagioclase in thin films and symplectites after omphacite are classified as oligoclase, with a high albite component ($X_{ab} = \frac{Na}{Na+Ca+K} = 0.80$ to 0.88), a moderate anorthite content ($X_{an} = \frac{Ca}{Na+Ca+K} = 0.12$ to 0.20) and a negligible orthoclase content ($X_{or} = \frac{K}{Na+Ca+K}$).

5.2 Trace and rare-earth elements

Mineral trace-element compositions of garnet, omphacite, amphibole and clinozoisite were obtained from a representative leucosome-absent sample (HO22-2; Fig. 5a, left) and a leucosome-bearing sample (HO23-1F; Fig. 5b). Rare-earth and most trace elements in most minerals show low concentrations close to or below the limits of detection (0.1–0.005 µg g^{-1}; Table S2).

The light rare-earth elements (LREEs) in garnet are below or next to the detection limit (Fig. S2a). The elements from Sm to Dy do not show pronounced zoning or even a slight increase from core to rim, whereas the heavy rare-earth elements (HREEs) display elevated contents in the core and decrease towards the rims (Table S2). Lithium, Ga, Zr and Ti contents are homogeneously distributed with < 1–2, 4–7, 1–5 and 200–300 µg g^{-1}, respectively.

Omphacite does not display compositional zoning within grains or for different textural settings and contains less than 1 µg g^{-1} of REEs (Fig. S2b). Omphacite in sample HO22-2 is significantly enriched in Li and impoverished in Mn compared to leucosome-bearing sample HO23-1F, measured with ∼ 60–80 vs. 15 µg g^{-1} and 140–160 vs. 230–270 µg g^{-1}, respectively. Titanium, V and Cr occur in noticeable amounts of ∼ 1000, 300–400 and 40–80 µg g^{-1}, respectively. Gallium is, despite the significantly lower Al_2O_3 content in omphacite compared to garnet, 3 to 5 times enriched with 12 to 24 µg g^{-1}.

Amphibole has very low REE contents, typically < 1 µg g^{-1} (Fig. S2c). Lithium concentration is significantly lower compared to omphacite (∼ 1–2 µg g^{-1}); Be and B are in the range of 1 to 5 µg g^{-1}, the highest values being measured in sample HO22-2. Strontium, Y and Zr contents are low with 12–26, 1–3 and 8–10 µg g^{-1}, respectively.

Clinozoisite is significantly enriched in most high-field-strength (HFS) and large-ion lithophile (LIL) elements (Fig. 8). Figure 8a shows the chondrite-normalized pattern of matrix and leucosome clinozoisite core–rim compositions. Matrix clinozoisite rims show the highest REE concentrations, while leucosome clinozoisite REE contents are not as systematically zoned. Clinozoisite is generally enriched in LREEs compared to HREEs (Frei et al., 2004), with rims showing higher concentrations compared to cores. Leucosome clinozoisite displays a comparable compositional trend but is significantly impoverished in REEs compared to the matrix variety. Sample HO22-2, which does not contain clear leucosome parts, shows particularly high REE contents in clinozoisite rims, approximately 10 times the leucosome-bearing sample. HFS elements such as Ti and Zr have distinctly higher concentrations in matrix clinozoisite compared to the leucosome mineral (Fig. 8b). Matrix clinozoisite always contains higher amounts of Mg, Ti, V and Cr, while leucosome clinozoisite has elevated contents in Sr and Pb (Fig. 8c–e; Table S2). Gallium does not correlate with the Al_2O_3 content of clinozoisite and is systematically lower in leucosome grains (Fig. 8f).

6 Petrological interpretation

In the eclogite matrix, all minerals show sharp grain boundaries when in mutual contact – in particular garnet, omphacite, hornblende and clinozoisite (Figs. 5a and 6a, b). This apparent textural equilibrium is interpreted to reflect an equilibrated eclogite-facies mineral assemblage. The relative abundance of hydrous minerals indicates high a_{H_2O} during equilibration (Miller, 1990), interpreted as fluid-saturated conditions close to the Eoalpine P_{max} (Bruand et al., 2010; Schorn et al., 2021; Rogowitz and Huet, 2021).

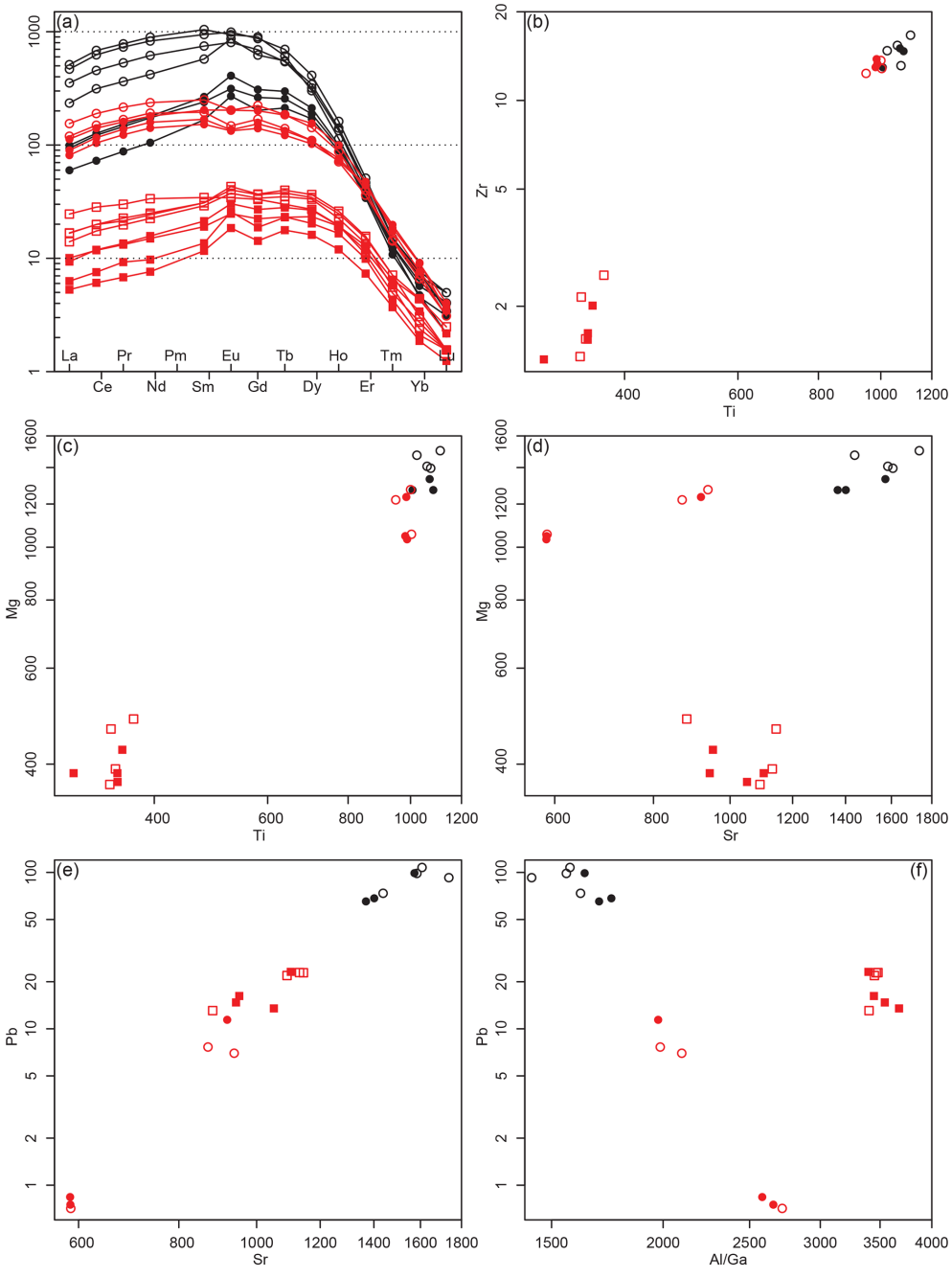

Figure 8. Clinozoisite trace-element data. **(a)** Chondrite-normalized rare-earth element spider plot. **(b–f)** Binary element plots. Black: sample HO22-2. Red: sample HO23-1F. Dots are matrix minerals, and squares are leucosome clinozoisite. Filled symbols are for cores, and empty ones are rims. Values are in $\mu g\,g^{-1}$.

The leucocratic segregations host the same mineral assemblage but are dominated by coarse-grained, subhedral-to-euhedral hornblende–clinozoisite–quartz with subordinated disseminations of garnet, omphacite and rutile. The similarity in major-element composition of the rock-forming minerals found in the rock matrix and leucosomes, as well as the general compositional REE trend for matrix vs. leucosome clinozoisite, indicates near equilibrium among the involved minerals. When considering the *zy* section of finite strain, the segregations are roughly concordant with the eclogite-facies foliation; they locally show hornblende-rich selvedges towards the rock matrix and lack abrupt termination (Figs. 3 and 4), in contrast to injected melts observed in similar eclogites (Fig. 1e; Schorn et al., 2021). Importantly, the rocks lack plagioclase except for thin films and local retrogression of omphacite. Assuming these textures

Table 2. X-ray fluorescence whole-rock analyses and model bulk composition for thermodynamic modelling.

Sample	Composition	SiO_2	TiO_2	Al_2O_3	Fe_2O_3	FeO^{tot}	MnO	MgO	CaO	Na_2O	K_2O	P_2O_5	LOI	O	Total	XFe^{3+}
HO21-1a	XRF (wt %)	48.11	1.46	14.88	10.89	–	0.18	8.21	12.29	2.84	0.05	0.17	0.47	–	99.54	–
HO21-1b		50.93	1.21	14.55	9.72	–	0.15	7.95	11.94	2.74	0.06	0.13	0.40	–	99.78	–
HO21-5		49.75	1.33	14.82	10.88	–	0.17	8.12	10.96	2.98	0.14	0.11	0.35	–	99.61	–
HO22-8		47.48	1.56	14.89	11.62	–	0.20	8.67	11.71	2.76	0.07	0.14	0.40	–	99.50	–
Avg XRF (wt %)		49.07	1.39	14.79	10.78	–	0.17	8.24	11.73[a]	2.83	0.08	0.14	0.41	–	99.61	–
Avg model bulk (mol %)		51.55	1.10	9.15	–	8.52	–	12.90	13.00[b]	2.88	0.05	–	–	0.84	100.00	0.20

[a] Whole-rock CaO. [b] Corrected for P_2O_5 in apatite ($CaO^{tot} - 3.33 \cdot P_2O_5$). FeO^{tot} is total iron expressed as FeO. O is oxygen, related to FeO via $2 \cdot FeO + O = Fe_2O_3$. Bulk O is equal to bulk Fe_2O_3. $XFe^{3+} = 2 \cdot O / FeO^{tot} = Fe^{3+} / (Fe^{3+} + Fe^{2+})$. LOI: loss on ignition.

formed at a later moment during exhumation, the macro- and microscopic aspects of the matrix–segregation pairs are interpreted in terms of minor prograde partial melting; limited melt segregation; and crystallization under eclogite-facies conditions, or at least within the stability field of omphacite. In our petrogenetic model, the hydrous eclogite assemblage experienced low degrees of melting at high a_{H_2O}, possibly in proximity to the fluid-present solidus. The inferred peak-pressure assemblage therefore is garnet–omphacite–hornblende–clinozoisite–quartz–rutile–silicate melt.

7 Phase diagram calculations

Phase equilibrium modelling was performed using an average composition of four whole-rock eclogite bulk compositions in order to constrain the first-order phase equilibrium topology. Calculations were carried out in the simplified 10-component Na_2O–CaO–K_2O–FeO–MgO–Al_2O_3–SiO_2–H_2O–TiO_2–O_2 (NCKFMASHTO) model system by omitting minor MnO and reducing the whole-rock CaO^{tot} to account for the presence of apatite. About 20 % of the total Fe is converted to Fe^{3+}, chosen to roughly reproduce the measured silicate X_{Fe}. Analysed whole-rock compositions and the model composition used for phase diagram calculations are listed in Table 2. Phase diagrams are presented in Fig. 9; note that for the calculated epidote–clinozoisite solid solution, we refer to clinozoisite (cz) for consistency.

7.1 Temperature–$M(H_2O)$ diagrams

In order to assess the effect of variable H_2O content, we begin with a T–$M(H_2O)$ diagram, calculated at a P_{max} of 20 kbar assuming a pure H_2O fluid at first (Fig. 9a). The modelled solid peak assemblage of garnet–omphacite–hornblende–clinozoisite–quartz–rutile (± calculated muscovite) is stable over a wide T–$M(H_2O)$ interval and is joined by free H_2O for $T < 720$ °C and $M(H_2O) > 1.5$ mol % (dotted region in Fig. 9a). At higher T, melt is predicted, with a narrow temperature interval where it coexists with free H_2O. The H_2O-absent solidus temperature gradually increases with decreasing $M(H_2O)$. Under suprasolidus conditions, additional H_2O enhances melt production, as shown by the contours for melt volume increasing with $M(H_2O)$ (Fig. 9a). For low $M(H_2O)$ (< 1.5 mol %–2 mol %), the assemblage becomes H_2O- and melt-absent and is bound by the sequential appearance of kyanite and the disappearance of hornblende and clinozoisite with decreasing $M(H_2O)$. A similar sequence occurs with increasing temperature, with the stabilization of kyanite followed by the consumption of clinozoisite and finally hornblende. A small amount of white mica ($\ll 1$ vol %) is predicted until it is exhausted towards high T and $M(H_2O)$. Assuming the rock contained $M(H_2O)$ corresponding to the average loss on ignition (LOI = 1.4 mol % H_2O, vertical black line), the inferred melt-bearing assemblage field (bold letters, white borders) is bound by the H_2O-present solidus and the appearance of kyanite towards low and high temperature, respectively, bracketing a narrow range of ∼ 720 to 740 °C at 20 kbar (Fig. 9a).

Under high-pressure–high-temperature conditions, aqueous fluids may dissolve, among others, significant amounts of silicate material (e.g. Manning, 2018). Therefore, we tentatively use the silicate-bearing aqueous fluid model of Holland et al. (2018) to explore the consequences of a composite metamorphic fluid. The respective T–$M(H_2O)$ pseudosection (Fig. 9b) is calculated at a slightly lower pressure of 19.5 kbar in order to preserve the phase relations as shown in Fig. 9a where pure H_2O was used. The diagrams are very similar, with the main difference being the displacement of the fluid-present solidus in Fig. 9b to about 750 °C. Because the chosen fluid model dissolves all considered system components, muscovite is consumed in the fluid-present assemblage fields (dotted region). The inferred melt-bearing equilibrium assemblage field (bold letters, white borders) is delimited by the same phase relations as before, albeit covering a slightly narrower temperature range of ∼ 750–760 °C at 19.5 kbar for an $M(H_2O)$ corresponding to the LOI (Fig. 9b).

7.2 Pressure–temperature diagrams

Closed-system pseudosections using 1.4 mol % H_2O (LOI) are presented in Fig. 9c and d. Note the different choice of fluid composition (pure H_2O vs. composite fluid). Since the phase relations are comparable, the main characteristics of the diagrams are described in conjunction.

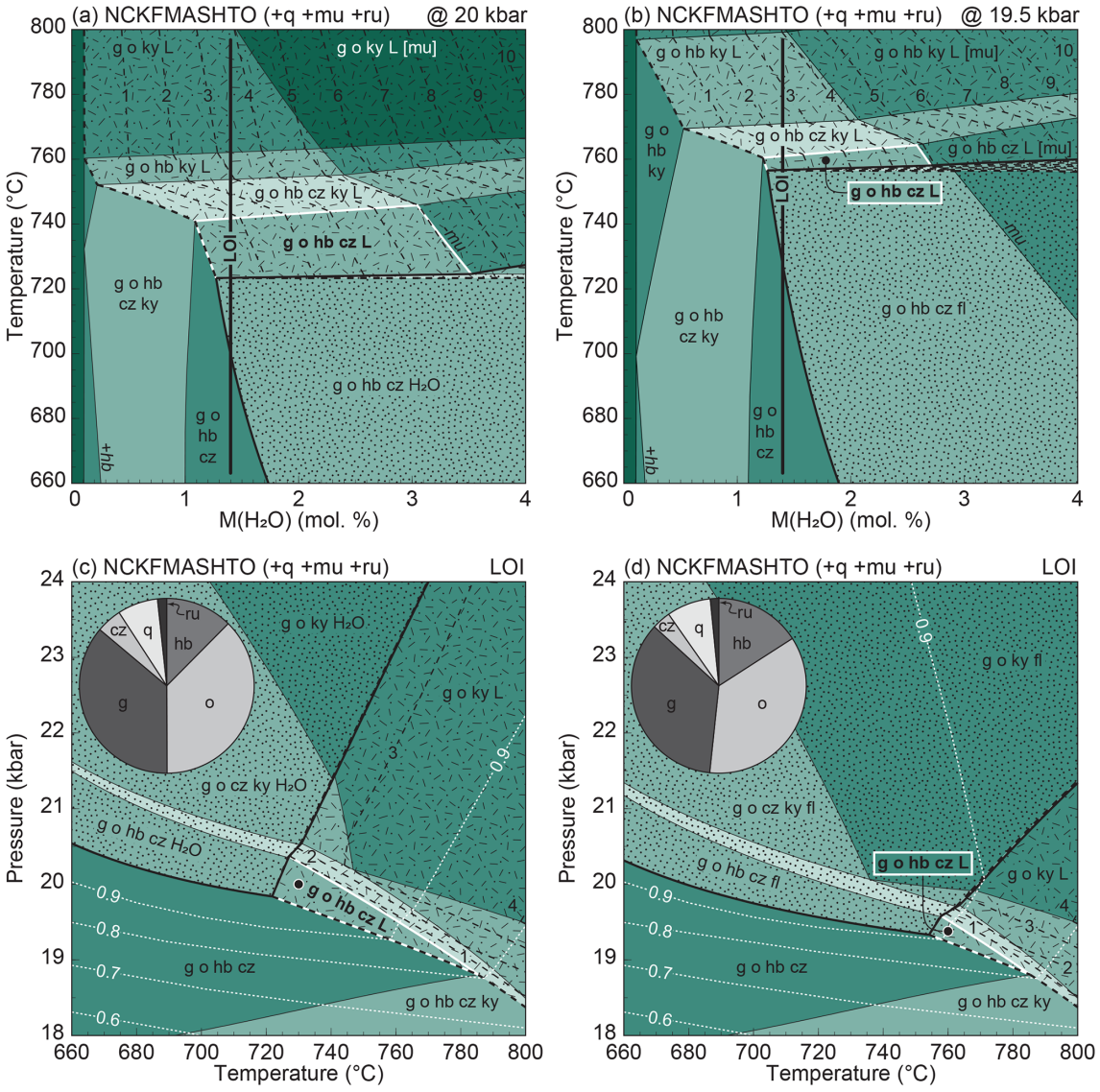

Figure 9. P–T–$M(H_2O)$ phase diagrams for average eclogite at Hohl. **(a, b)** T–$M(H_2O)$ pseudosection calculated at 20 and 19.5 kbar, respectively. The black line corresponds to $M(H_2O)$ corresponding to the LOI (1.40 mol % H_2O) set in **(c, d)** P–T pseudosections. The inferred equilibrium assemblage is written in bold, and the respective field is highlighted with a white border. Bold field boundaries and dotted shading highlight H_2O-/fluid-saturated assemblage fields. The bold dashed line is the solidus, and dash-dotted shading marks melt-bearing fields. Dashed lines are contours for melt percentage (vol %), and dotted white lines in **(c)** and **(d)** are contours for a_{H_2O}. Pie charts give the phase modes (vol %) calculated at the black dots in **(c)** and **(d)**: garnet, ∼ 36; omphacite, ∼ 35; hornblende, ∼ 15; quartz, ∼ 7; clinozoisite, ∼ 4; rutile, ∼ 1; white mica, ∼ 0.5 (not labelled); tonalitic melt, ∼ 0.5 (not labelled). Note that in **(a)** and **(c)**, fluid is H_2O, whereas in **(b)** and **(d)**, fluid is silicate-bearing. Clinozoisite (cz) refers to the binary epidote–clinozoisite solid solution.

Similarly to Fig. 9a and b, the diagrams consist of three main sections in P–T space: a low-T side where free H_2O/fluid is stable, a high-T part where melt is predicted and a low-P area where no liquid phase is calculated (Fig. 9c, d). The stabilization of kyanite towards high pressure is followed by the demise of hornblende and finally by the breakdown of clinozoisite, leaving a nominally anhydrous solid assemblage (except for negligible amounts of muscovite) in the presence of free H_2O/fluid or melt. Contours for a_{H_2O} show a steady decrease away from the H_2O/fluid saturation line (dotted white lines in Fig. 9c, d). Because the fluid model considers dissolved silicate material, a_{H_2O} is always below unity in the fluid-saturated region (Fig. 9d). Note that within the H_2O-/fluid-present fields, the maximum calculated amount of free aqueous fluid does not exceed ∼ 1 vol % while H_2O-/fluid-absent fields are identical in both diagrams. The melt-bearing peak assemblage field (bold labels, white border) is wedge-shaped and delimited by the introduction of kyanite and loss

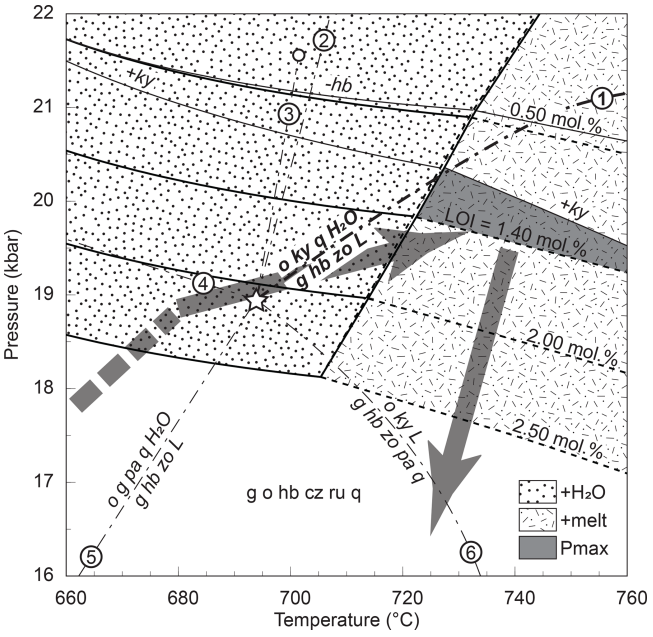

Figure 10. Simplified NCKFMASHTO phase assemblage diagram for average eclogite composition and variable $M(H_2O)$. The H_2O saturation line is solid black, and the solidus is dashed. The kyanite-in line is calculated for $M(H_2O) = \text{LOI}$ (1.40 mol %); the hornblende-out line towards high pressure is calculated for low $M(H_2O)$ (0.50 mol %). All assemblage fields additionally contain minor muscovite, and the fluid is pure H_2O. The grey arrow is a potential P–T path culminating at the inferred P_{max} conditions (grey field). Dash-dotted lines show the underlying phase relations in the simplified NCFMASH (Na_2O–CaO–FeO–MgO–Al_2O_3–SiO_2–H_2O) model system emanating from an invariant point (white star). Reaction (R1) is [pa] and highlighted in bold. Reaction (R2): [zo] $g + o + pa + q + H_2O = hb + ky + L$. Reaction (R3): [hb] $g + o + zo + pa = ky + L$. This line terminates in the MgO-free subsystem (white dot). Reaction (R4): [L] $g + hb + zo + pa + q = o + ky + H_2O$. Reaction (R5): [ky]. Reaction (R6): [H_2O]. The [g], [o] and [q] reactions are omitted.

of melt towards high and low pressure, respectively, and by the H_2O-/fluid-present solidus towards low temperature. Considering pure H_2O a fluid phase, the field is stable between ∼ 720–780 °C and 18.5–20.5 kbar (Fig. 9c), whereas it lies between ∼ 750–780 °C and 18.5–20 kbar when the fluid model is used (Fig. 9d). Within this field, the modelled mineral modes remain nearly unchanged (pie charts calculated at the black dots with white outlines in Fig. 9c, d) and < 1 vol % melt is predicted.

8 Discussion

8.1 Petrogenetic model

The eclogites at Hohl host a well-equilibrated high-pressure assemblage including a variable amount of hydrous hornblende and clinozoisite, consistent with equilibration at high a_{H_2O}. Phase equilibrium modelling assuming conservative estimates for $M(H_2O)$ predicts aqueous fluid and/or hydrous silicate melt coexisting with the solid eclogite assemblage at well-established Eoalpine P_{max} conditions (21 ± 3 kbar and 680–740 °C; Figs. 2 and 9c, d). Inclusions of hornblende in cores of large garnets (Fig. 6a) suggest that the protoliths were hydrated at some point along the prograde path. In this scenario, modelling allows us to bracket the minimum and, less so, the maximum $M(H_2O)$ of the eclogites at Hohl. Assuming the rocks contained ∼ 2–3 mol % H_2O on the prograde path, they would become fluid- or melt-bearing around 18 kbar, depending on temperature (Figs. 10 and 11). Progressive dehydration and fluid loss lead to a decrease in $M(H_2O)$, thereby shifting the calculated H_2O-/melt-present fields towards conditions of higher P–T without altering the calculated solid equilibrium assemblage (Fig. 10). However, if the overall $M(H_2O)$ is less than ∼ 1.4 mol % (LOI), kyanite is predicted by the calculations but not found in our samples. At even lower $M(H_2O)$ (≤ 0.5 mol %), hornblende would no longer be part of the calculated mineral assemblage (Fig. 10). On the other hand, if the rocks were hydrated at much lower P–T, they would dehydrate along a larger portion of the prograde path without affecting the evolution near P_{max}. The minor calculated white mica ($\ll 1$ vol %) is regarded as a modelling artefact without petrological meaning.

In our preferred scenario, the prograde path terminated at around 20 kbar and 700–750 °C, with about 1.4 mol % H_2O (LOI) stored in the mineral assemblage. Note that our modelling does not allow for a refined estimate of the established Eoalpine P_{max} for the area, nor do we invoke substantially different (P–)T conditions. We consider equilibration conditions that are consistent with those reported in the literature, albeit shifted to somewhat higher temperature if the fluid model is used (Fig. 9d). The uncertainty involved in thermodynamic modelling does not allow us to confidently establish whether the rocks were fluid-present throughout; however our calculations suggest that a_{H_2O} was near unity ($0.8 < a_{H_2O} < 1.0$; Fig. 9c, d) around the inferred peak conditions regardless of whether an aqueous fluid was present or not. The robustness of our assumptions is further corroborated by calculated mineral modes that are consistent with the studied thin sections and rather insensitive to P–T changes within the uncertainty of the inferred peak assemblage field (pie charts in Fig. 9c, d).

Accepting limited dehydration and equilibration at or close to P_{max} (Fig. 11a), we propose the eclogites experienced minor melting (Fig. 9c, d). The resulting melt phase is expected to be rich in H_2O (≥ 15 wt %–20 wt %; Hermann et al., 2006; Laurie and Stevens, 2012) and have a comparatively low viscosity. Enhanced element transport within the melt phase located at grain boundaries promoted grain growth and the formation of coarse-grained euhedral crystals (Fig. 11b; Miyazaki et al., 2016). Partial dismemberment of the nearby eclogite matrix occurred, as indicated by

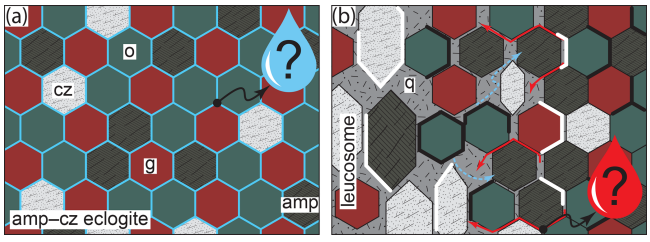

Figure 11. Sketch summarizing the proposed petrogenetic evolution of leucosome-bearing eclogites at Hohl (adapted from Wohlers and Baumgartner, 2013). **(a)** Prograde- to P_{max} equilibration in the presence of fluid (blue). **(b)** Incipient melting, partial dismemberment of matrix and leucosome formation close to P_{max} (21 ± 3 kbar and 680–740 °C). Drops indicate fluid (blue) and melt (red) potentially being extracted from the rock. Red arrows indicate melt feeding from the matrix into the leucosome. Blue arrows symbolize H_2O released from melt to form amphibole-rich selvedges. Thick white and black lines symbolize plagioclase films and symplectites, respectively, forming at lower pressure.

the disseminations of garnet, omphacite and rutile within the leucosomes (Fig. 5b; cf. Wohlers and Baumgartner, 2013). The melt is suggested to have locally accumulated in low-pressure extensional zones (e.g. boudin necks; Fig. 4b). However, we posit that at no point did the melt pond sufficiently for it to segregate into an isolated compositional domain, consistent with limited low-pressure retrogression. As such, closed-system modelling may not be perfectly accurate, but we regard the main phase diagram topology to be preserved, and the melts crystallized close to the peak-pressure conditions following minor decompression across the solidus (Figs. 10 and 11). Excess H_2O dissolved in the melt is thereby released, and by reacting with the surrounding rock matrix, it is suggested to form the hornblende-rich selvedges that locally bind the leucosomes (Figs. 4, 5b and 11b). Subsequently, the rocks underwent near-isothermal decompression to mid-crustal conditions. The thin layers of plagioclase and amphibole found next to large hornblende and/or clinozoisite close to the leucosomes (Fig. 5c) may be due to (i) solid–solid reaction within local compositional domains, (ii) fluid-assisted growth and partial equilibration due to reaction with a late-stage fluid, and/or (iii) crystallization of melt vestiges adhering to grain boundaries (i.e. pseudomorphs after melt-filled pores; Holness and Sawyer, 2008). We do not insist on one explanation as all may be applicable; however we suggest that the timing of plagioclase growth is similar to that of symplectite formation at the expense of omphacite, with the two processes possibly being related (Fig. 11b).

8.2 Fluid- vs. melt-related origin of segregations

Under high-pressure–high-temperature conditions, aqueous fluids can dissolve large quantities of solids (in particular SiO_2) and may reach complete miscibility with hydrous melt at the second critical endpoint. However, the interval where transitional solute-rich fluids exist is considered narrow (50–100 °C; Hermann et al., 2006) and lies at UHP conditions in the K_2O-bearing basalt–H_2O system (~ 770 °C and 34 kbar; Mibe et al., 2011) that were clearly not reached at the eclogite type locality. Precipitation and/or recrystallization from a solute-rich fluid is a possibility, although this typically produces high-variance assemblages such as quartz, quartz–phengite or quartz–kyanite in veins documented in similar eclogites (Miller, 1990). It is ultimately impossible to confidently differentiate between a fluid- or melt-related genesis of the documented segregations; however, it is plausible that both aqueous fluid and hydrous melt participated in their formation. When minor K_2O–TiO_2–O_2 are ignored, the compositional system is reduced to the core metabasite model system of Na_2O–CaO–FeO–MgO–Al_2O_3–SiO_2–H_2O (NCFMASH). The thin-section paragenesis then simplifies to the quadrivariant assemblage of garnet (almandine–pyrope–grossular), omphacite (diopside–hedenbergite–jadeite), hornblende s.s., quartz and pure zoisite instead of Fe^{3+}-bearing clinozoisite. Together with free H_2O, melt, kyanite and end-member paragonite, the assemblage becomes invariant, with the respective point calculated at about 19 kbar and 690 °C (white star in Fig. 10). From there the paragonite-absent reaction

$$\text{omphacite} + \text{kyanite} + \text{quartz} + H_2O = \text{garnet} + \text{hornblende} + \text{zoisite} + \text{melt} \quad \text{(R1)}$$

emanates towards high pressure and temperature, falling close to/within the inferred P_{max} equilibration conditions (Fig. 10). While we have not found kyanite in our thin sections, it is a common minor constituent in more aluminous eclogites at Hohl and in the Saualpe area (Miller et al., 1988; Miller, 1990; Bruand et al., 2010; Miladinova et al., 2022). As such, it is possible that following prograde dehydration, minor kyanite was consumed together with aqueous fluid in favour of the leucosome assemblage with hornblende, zoisite (in lieu of Fe^{3+}-bearing clinozoisite), minor garnet and melt as schematically represented by Reaction (R1) in Fig. 10. Alternatively, invoking the kyanite-absent reaction, Reaction (R5), paragonite would be required as a reactant (Fig. 10). According to Miller (1990), the latter exclusively occurs in kyanite-bearing eclogites and may have been consumed similarly to kyanite during the prograde evolution. The other reactions would either require the absence of a key mineral or produce kyanite as a peritectic phase (or both), making them unsuitable for the documented petrological evolution. In any case, when H_2O is involved as a reactant, experiments have shown that clinopyroxene and quartz are the main solid participants in wet melting of eclogite (Laurie and Stevens, 2012), consistent with our proposed melting in Reaction (R1).

The observed systematic differences in trace-element and rare-earth-element composition of clinozoisite in the matrix

and leucosome may provide further clues to the main petrogenetic process involved in their formation (Fig. 8). In terms of major elements, the leucosome clinozoisite is distinctly impoverished in Fe^{3+} compared to the matrix variety, indicating crystallization of the former in an fO_2-rock-buffered system where the redox budget is bound to the residuum, in particular in the matrix clinozoisite. Similarly, high-field-strength elements are difficult to mobilize in a fluid phase unless certain agents such as fluorine and chlorine favour their dissolution via complexation (e.g. Rapp et al., 2010). Elevated contents of F and Cl in a hypothetical fluid phase can however be excluded in our samples as all hydrous phases lack these elements in significant amounts. The chondrite-normalized REE patterns of clinozoisite (Fig. 8a) show lower enrichment in leucosome clinozoisite and high to very high contents for matrix clinozoisite, with the highest concentrations measured in clinozoisite from the sample without any noticeable leucosomes (HO22-2). In the bivariate Ti-versus-Zr plot (Fig. 8b), the same behaviour is observed. In most cases there is also a systematic difference between core and rim composition, where the rims are more enriched in HFSE. While the REEs replace Ca, the elements Zr and Ti substitute the [Al,Fe^{3+}]-crystallographic site in clinozoisite. Both display the same trend in clinozoisite (Fig. 8). Large-ion lithophile elements can be easily mobilized by an aqueous fluid, and hence high contents are expected in leucosome clinozoisite. Figure 8d and e show bivariate Sr–Mg and Sr–Pb diagrams, respectively, where the leucosome-absent sample HO22-2 has the highest Sr, Pb and Mg contents and the leucosome clinozoisite intermediate Sr and Pb and low Mg concentrations. Matrix clinozoisite has the lowest Sr and Pb contents but intermediate Mg values. Strontium and Pb enter the Ca site, while Mg occupies the [Al,Fe^{3+}] position in clinozoisite. The observed LILE pattern is therefore not fully compatible with a purely subsolidus fluid-assisted mobilization and recrystallization. To further explore the potential formation process(es) of the leucosome clinozoisite, we interrogate the Al / Ga ratio in clinozoisite (Fig. 8f). Both elements occur as 3+ cations in silicates and have a similar geochemical behaviour. However, the ionic diameter of Al is about 15 % smaller; hence it has a higher ionic potential and should be slightly less mobile in a fluid phase compared to Ga (Goldschmidt, 1926). The Al / Ga ratio in clinozoisite from the Hohl eclogite varies between ca. 1500 and ca. 4000, with the leucosome clinozoisite having the highest ratios (Fig. 8f). Compared to an average basalt Al / Ga ratio of ∼ 4700 (Turekian and Wedepohl, 1961; Vinogradov, 1962), the analysed clinozoisite shows a systematically lower ratio, which cannot be explained solely by a fluid-assisted process as the ratio should be lowest in leucosome clinozoisite in this case. Omphacite and amphibole have Al / Ga ratios comparable to that of the ideal whole rock (ca. 4000; Table S2), while garnet has distinctly higher ratios of 15 000 to 30 000 (Table S2). We interpret this in terms of Ga being preferentially partitioned into clinozoisite during prograde clinozoisite and garnet growth. Igneous plagioclase is seen as the main Al- and Ga-bearing precursor phase to clinozoisite, thus donating all its Ga to the newly formed mineral, with prograde garnet growth involving igneous/early metamorphic clinopyroxene and possibly amphibole.

Clearly, the actual processes involved in the formation of the described features are multivariant and complex. However, in light of petrography, homogeneous mineral compositions among matrix–segregations, and trace HFSE and LILE behaviour, we prefer a petrogenetic model involving minor melting of the hydrous eclogite assemblage, forming a nearly water-saturated melt which is accompanied by increased element mobility and transport within the melt phase at the grain boundaries and favouring grain growth and the formation of the documented pegmatitic textures.

8.3 Amphibole–clinozoisite eclogites as source for injected melts?

Schorn et al. (2021) describe similar pegmatitic segregations hosted in clinozoisite-bearing eclogite located in the high-pressure unit of the Saualpe, some 40 km west of the locality studied here (Fig. 1b). Their segregations also host centimetre-sized euhedral hornblende–clinozoisite–quartz but additionally contain significant amounts of Na-rich plagioclase, indicating crystallization at sub-eclogite-facies pressure. Furthermore, these pegmatoids are, unlike the leucosomes described here, discordant to the high-pressure foliation of the host eclogite and display abrupt terminations (Fig. 1e). The authors interpret the pegmatoids as injected crystallized melts produced in a nearby eclogitic source due to fluxing via metapelite-derived aqueous fluid after near-isothermal exhumation to the middle crust. In light of the findings presented here, we suggest an alternative mechanism for pegmatoid formation, complementary to the scenario described in Schorn et al. (2021). If the melts invoked in our model were allowed to be extracted from the source rocks and accumulate in melt-rich pockets, they would eventually form a distinct H_2O-rich compositional system. As such, the pockets would not solidify prior to cooling and decompression below the wet basalt solidus under conditions of lower P–T – conditions that are consistent with the inferred pegmatoid crystallization at ∼ 700 °C and 8–10 kbar (Fig. 2; Schorn et al., 2021). As such, we propose that if similar melts were to be sufficiently accumulated, they might represent, in part, parent melts to pegmatitic segregations like those described in Schorn et al. (2021). This scenario requires efficient melt transfer out of the source rocks, which may be facilitated by very low melt viscosity, a deformation-assisted melt extraction mechanism and/or more voluminous melt production beyond a critical fraction (∼ 0.07; Rosenberg and Handy, 2005) in the presence of deformation (e.g. Kohlstedt and Holtzman, 2009). More enhanced high-pressure melting, but without invoking unreasonably high temperatures (≤ 750 °C), might be favoured by a more fertile protolith

such as phengite-rich rocks (Schmidt et al., 2004) or by fluxing agents in the metamorphic fluid (e.g., H_2O and F; Baker and Vaillancourt, 1995).

8.4 Enhanced melt production due to dehydration of refractory eclogites?

Whereas the investigated samples have an identical mineral assemblage, there is some variability in the bulk rock chemistries (Table 2) that propagates to the observed mineral modes and compositions – compare the relatively amphibole–clinozoisite-poor true eclogite on the left-hand side of Fig. 5a with the amphibole-rich variety shown on the right-hand side. Phase diagram modelling of two compositional end-members (model bulks given in the Supplement, Table S3) shows that whereas the main phase relations are the same as discussed above, melting is predicted at slightly different temperatures (Fig. 12a). Applying the same modelling considerations as above (apatite correction, $X\mathrm{Fe}^{3+} = 0.20$, pure H_2O fluid) and $M(H_2O)$ sufficient to saturate the bulk compositions at high pressure, the more fertile composition (HO21-5) starts melting a few degrees Celsius lower than the H_2O-present solidus temperature of the more refractory sample HO22-8 at the same pressure (Fig. 12a). Thus, there is a theoretical P–T range where the fertile rock is melting while the refractory one is still subsolidus but dehydrating (green field in Fig. 12a). There, the chemical potentials of H_2O (μH_2O) can be directly compared due to the relationship of the conjugate intensive–extensive variables μH_2O–$M(H_2O)$ (Powell et al., 2005). This is shown by the dashed lines in Fig. 12a, contouring the diagram for the gradient in chemical potential ($\Delta\,\mu H_2O$) between the rocks. Positive values indicate a gradient in μH_2O from the refractory to the fertile sample; negative values mean a gradient in the opposite direction. The green shading therefore corresponds to the most favourable conditions for H_2O transfer among neighbouring compositional layers, marking where both free H_2O and appropriate gradients in chemical potential coexist. Using this schematic approach, it is not possible to quantify the actual amount of H_2O that might be transferred or to estimate the length scales over which such a transfer process may be efficient. However, in light of aqueous fluid being highly mobile, we suggest this mechanism may operate at the outcrop scale (dm–m), facilitating fluid transfer between rocks with contrasting μH_2O, or a_{H_2O}, as proposed for neighbouring layers of refractory vs. fertile granulites (Waters and Whales, 1984).

The P–T conditions where fluid- and melt-present assemblages, respectively, coexist to enable this process are narrow (Fig. 12a). When additional compositional variability, such as the bulk oxidation state, is considered, the potential (P–)T field may be enlarged. This effect is explored via an isobaric T–$X\mathrm{Fe}^{3+}$ pseudosection calculated at 20 kbar, using the average eclogite composition (Table S3; Fig. 12b). The diagram covers a range of 680 to 780 °C and $X\mathrm{Fe}^{3+}$ of 0 to 0.8, with $M(H_2O)$ chosen to just saturate the calcu-

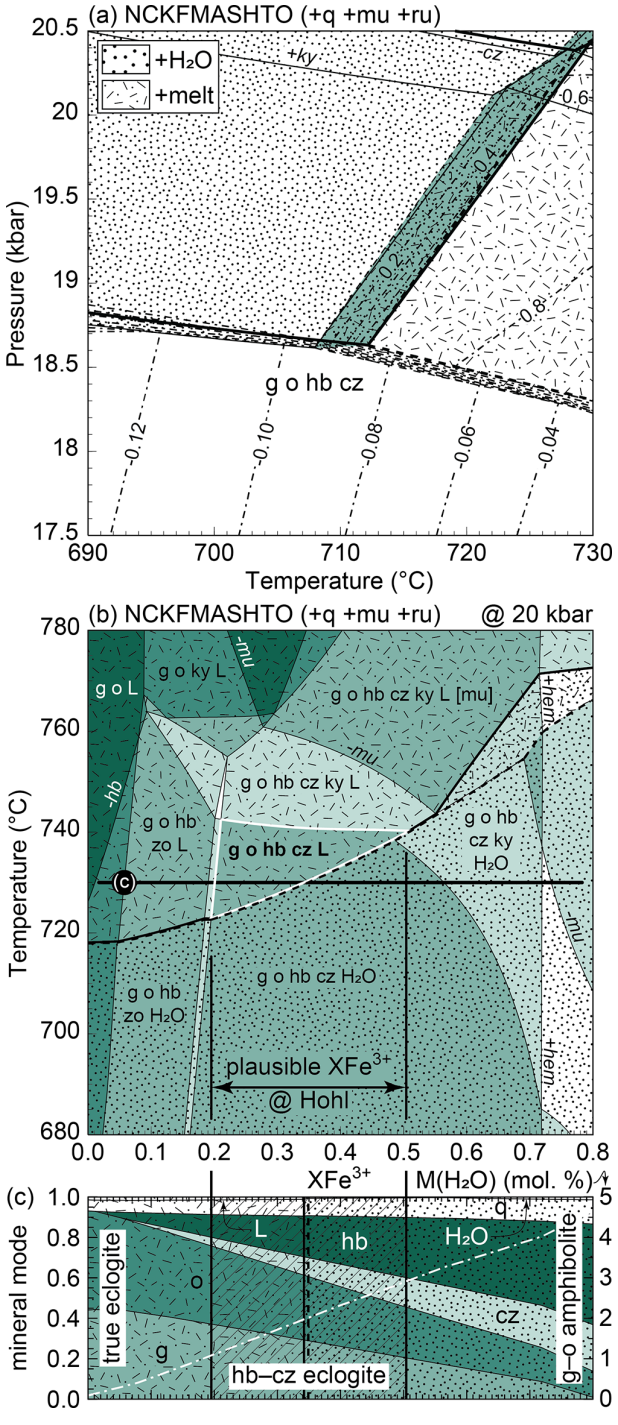

Figure 12. **(a)** Key phase relations for refractory (HO22-8, thick lines) and fertile (HO21-5, thin lines) eclogite sample at P_{max}. Dashed contours are $\Delta\,\mu H_2O$ (kJ mol^{-1}) between the two samples. **(b)** T–$X\mathrm{Fe}^{3+}$ diagram for hydrated average eclogite calculated at 20 kbar. The inferred equilibrium assemblage is written in bold, and the respective field is highlighted with a white border. The isothermal black line is for **(c)**. **(c)** Modebox calculated at 730 °C. Zoisite and clinozoisite are grouped; muscovite, kyanite, rutile and hematite are omitted for clarity (< 3 vol % in sum). The dash-dotted white line gives the mineral-bound H_2O (mol %). The thick dashed line is the solidus, and the thick solid line is the H_2O saturation line. Shading indicates the presence of melt and/or free H_2O.

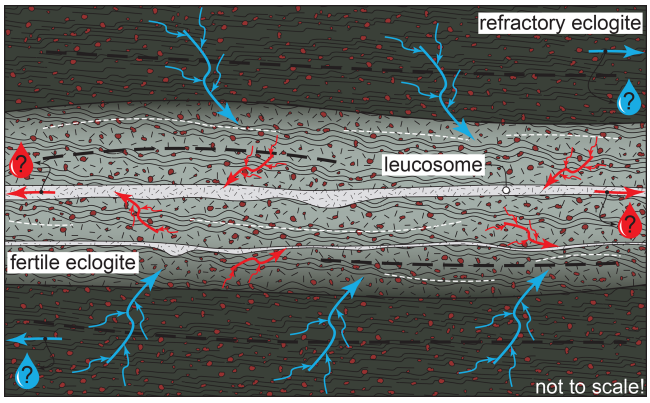

Figure 13. Drawing summarizing our suggested interplay between refractory and fertile eclogite layers around P_{max}. Blue and red arrows symbolize fluid and melt transfer, respectively. The arrow size indicates the scale of flux. Drops symbolize possible fluid/melt extraction (see text). Dashed black lines are the foliation; dashed white lines indicate thin leucosomes.

lated assemblages at the lower temperature limit. Crucially, the wet solidus is displaced from a minimum of ∼ 720 °C at low $X\mathrm{Fe}^{3+}$ to about 760 °C for a high $X\mathrm{Fe}^{3+}$ of ∼ 0.8, separating H_2O- and melt-bearing assemblage fields at low and high temperature, respectively (Fig. 12b).

For the eclogites at Hohl and the preferred P–T conditions, the inferred equilibrium assemblage (garnet–omphacite–hornblende–clinozoisite–quartz–rutile–silicate melt) is confined to ∼ 720–740 °C, bracketed by the wet solidus and the appearance of kyanite at high T or $X\mathrm{Fe}^{3+} > 0.5$ (Fig. 12b). More reducing conditions ($X\mathrm{Fe}^{3+} < 0.2$) lead to the stabilization of end-member zoisite instead of a binary epidote–clinozoisite solid solution; however it is unlikely that the two actually coexist in natural rocks as predicted by the modelling. As such, a T ranging between 720–740 °C with $0.2 < X\mathrm{Fe}^{3+} < 0.5$ at 20 kbar is deemed a plausible range for the investigated samples (Fig. 12b; cf. Rebay et al., 2010).

The calculated modebox in Fig. 12c demonstrates that reducing conditions favour garnet–omphacite-dominated assemblages (true eclogites) such as sample HO22-2 (Fig. 5a, left), while additional Fe^{3+} is accommodated in increasing amounts of hydrous hornblende and clinozoisite – which is similar to sample HO21-1b (Fig. 5a, right). Accordingly, increasingly oxidizing conditions cause an incremental mineral-bound H_2O (dash-dotted white line in Fig. 12c), making these rocks more efficient fluid sources as they dehydrate. Counter-intuitively, however, such garnet–omphacite "amphibolites" that are rich in hydrous minerals show higher calculated wet solidus temperatures due to lowered bulk Fe^{2+} / Mg ratios. This is consistent with the minerals showing slightly higher X_{Fe} and lower $X\mathrm{Fe}^{3+}$ in true eclogite samples (e.g. HO22-2) compared to garnet–omphacite "amphibolites" (e.g. HO23-1F; see mineral chemistry).

Modelling suggests that while keeping composition otherwise constant, a variable bulk oxidation state can cause dehydration or melting of eclogite at the same pressure and temperature. In other words, oxidized layers may dehydrate to provide additional fluid to reduced ones, given they lie within the appropriate length scale of fluid transfer. Within this paradigm, hydrated eclogites next to rather dry ones constitute a source–sink couple driven by gradients in chemical potential between dehydrating and melting rocks (Waters and Whales, 1984), with fluid transfer from refractory eclogite layers towards their more fertile neighbours, potentially enabling fluid-fluxed melting (Fig. 13; Tafur and Diener, 2020). It should be noted that for moderate melt production (≤ 10 vol %), the main phase topology remains unchanged (Fig. 9a, b), except for the modelled disappearance of muscovite – which is not found in the first place. Subsequent melt loss would therefore preserve the observed eclogite-facies mineral assemblage, thereby obscuring the complex metamorphic evolution. If fluid-fluxed melting is rejected, variable degrees of prograde dehydration melting controlled by the natural compositional variability at the outcrop scale are envisaged as an alternative underlying petrogenetic process for the observations presented here.

9 Conclusions

Amphibole–clinozoisite eclogite from the Koralpe hosts centimetre-thick, concordant, laterally continuous leucocratic segregations of pegmatitic hornblende–clinozoisite–quartz and disseminations of matrix garnet–omphacite–rutile. Petrographic data and phase diagram modelling are interpreted in terms of prograde dehydration followed by limited melting at or close to the Eoalpine pressure maximum (21 ± 3 kbar and 680–740 °C). Enhanced element mobility in the melt phase favoured the crystallization of coarse-grained minerals, with limited melt accumulation allowing solidification near P_{max} conditions. H_2O exsolved from the melt formed amphibole-rich selvedges locally bounding the leucosomes towards the rock matrix. Final melt vestiges may have crystallized at lower pressure, forming thin films of plagioclase and/or amphibole. Alternatively, these textures formed via secondary fluid-related processes, similarly to retrogression of omphacite. In terms of melt mechanism(s), the natural variability in rock composition leads to contrasting mineral compositions and modes that in turn control the calculated solidus temperature at the outcrop scale. Using the bulk oxidation state as a compositional variable, thermodynamic modelling shows that oxidized layers are characterized by hydrous amphibole–clinozoisite-rich assemblages and an elevated H_2O-present solidus (∼ 740 °C at 20 kbar) compared to more reduced true eclogites which are dominated by nominally anhydrous garnet–omphacite that commence partial melting at slightly lower temperatures (∼ 720 °C) at the same pressure. Interlayering of such eclog-

ites may constitute a fluid source–sink couple in the appropriate conditions bracketed by the calculated solidi, favouring fluid transfer from dehydrating to neighbouring melt-bearing layers driven by gradients in the chemical potential of H_2O. In this scenario, aqueous fluid released from refractory layers causes fluid-fluxed melting of more fertile compositions, provided they lie within the appropriate length scale of fluid transfer (dm–m). For moderate melt fractions (≤ 0.10), the calculated solid thin-section assemblage (hornblende–clinozoisite–garnet–omphacite–quartz–rutile) is preserved, provided the resulting hydrous melts were extracted and segregated elsewhere. Crystallization of these melt-rich domains would occur at lower pressure and possibly be related to similar eclogite-hosted pegmatitic segregations documented in the Saualpe (Schorn et al., 2021). However, given the overall small melt fractions, far-field transport of the melt is implausible. Eclogites with comparable composition and pressure–temperature evolution are therefore unlikely contributors to significant arc magmatism in collisional settings.

Data availability. The data that support the findings of this study are available in this article; further information is available from the corresponding author upon reasonable request.

Supplement. The supplement related to this article is available online at: https://doi.org/10.5194/ejm-35-715-2023-supplement.

Author contributions. SiS: conceptualization, investigation, formal analysis, writing (original draft), visualization, resources and funding acquisition. AR: investigation, formal analysis, writing (review and editing), resources and funding acquisition. CH: investigation, formal analysis, writing (review and editing) and resources.

Competing interests. The contact author has declared that none of the authors has any competing interests.

Disclaimer. Publisher's note: Copernicus Publications remains neutral with regard to jurisdictional claims in published maps and institutional affiliations.

Special issue statement. This article is part of the special issue "(Ultra)high-pressure metamorphism, from crystal to orogenic scale". It is a result of the 14th International Eclogite Conference (IEC-14) held in Paris and Lyon, France, 10–13 July 2022.

Acknowledgements. Discussions with Jörg Hermann, Thomas Pettke and Michael Brown during the International Eclogite Conference (Lyon, 2022) helped clarify the ideas presented here. Suggestions and informal reviews of early versions of this paper by Lukas Baumgartner and Eleanor Green are thankfully acknowledged. We thank David Hernández-Uribe and the anonymous reviewer for their thorough reviews and Samuel Angiboust and Christian Chopin for their careful editorial handling.

Financial support. This research has been supported by the Austrian Science Fund (grant nos. P-33002-N to Simon Schorn and P-36034-N to Anna Rogowitz).

Review statement. This paper was edited by Samuel Angiboust and reviewed by David Hernandez-Uribe and one anonymous referee.

References

Baker, D. R. and Vaillancourt, J.: The low viscosities of $F + H_2O$-bearing granitic melts and implications for melt extraction and transport, Earth Planet. Sc. Lett., 132, 199–211, 1995.

Boynton, W. V.: Cosmochemistry of the rare earth elements: meteorite studies, in: Developments in geochemistry, Elsevier, https://doi.org/10.1016/B978-0-444-42148-7.50008-3, 1984.

Bruand, E., Stüwe, K., and Proyer, A.: Pseudosection modelling for a selected eclogite body from the Koralpe (Hohl), Eastern Alps, Mineral. Petrol., 99, 75–87, 2010.

Cao, W., Gilotti, J. A., Massonne, H.-J., Ferrando, S., and Foster, C. T. J.: Partial melting due to breakdown of an epidote-group mineral during exhumation of ultrahigh-pressure eclogite: An example from the North-East Greenland Caledonides, J. Metamorph. Geol., 37, 15–39, 2018.

Cao, W., Gilotti, J. A., and Massonne, H.-J.: Partial melting of zoisite eclogite from the Sanddal area, North-East Greenland Caledonides, Europ. J. Mineral., 32, 405–425, 2020.

Cao, W., Massonne, H.-J., and Liang, X.: Partial melting due to breakdown of phengite and amphibole in retrogressed eclogite of deep Precambrian crust: An example from the Algonquin terrane, western Grenville Province, Canada, Precambrian Res., 352, 105965, https://doi.org/10.1016/j.precamres.2020.105965, 2021.

Carswell, D. A.: Eclogite-facies Rocks, chap. Eclogites and the eclogite facies: definitions and classification, 1–13, Blackie, Glasgow, Springer Dordrecht, ISBN 9401092656, 1990.

Dachs, E.: PET: petrological elementary tools for mathematica, Comput. Geosci., 24, 219–235, 1998.

Deng, L.-P., Liu, Y.-C., Gu, X.-F., Groppo, C., and Rolfo, F.: Partial melting of ultrahigh-pressure metamorphic rocks at convergent continental margins: Evidences, melt compositions and physical effects, Geosci. Front., 9, 1229–1242, 2018.

Droop, G. T. R.: A general equation of estimating Fe^{3+} concentrations in ferromagnesian silicates and oxides from microprobe analyses using stoichiometric constraints, Mineral. Mag., 51, 431–435, 1987.

Feng, P., Wang, L., Brown, M., Johnson, T. E., Kylander-Clark, A., and Piccoli, P. M.: Partial melting of ultrahigh-pressure eclogite by omphacite-breakdown facilitates exhumation of deeply-subducted crust, Earth Planet. Sc. Lett., 554, 116664, https://doi.org/10.1016/j.epsl.2020.116664, 2021.

Frei, D., Liebscher, A., Franz, G., and Dulski, P.: Trace element geochemistry of epidote minerals, Rev. Mineral. Geochem., 56, 553–605, 2004.

Froitzheim, N., Plašienka, D., and Schuster, R.: Alpine tectonics of the Alps and Western Carpathians, in: The Geology of Central Europe. Volume 2: Mesozoic and Cenozoic, https://doi.org/10.1144/CEV2P.6, 2008.

Goldschmidt, V. M.: Crystal structure of rutile type with remarks on the geochemistry of the bivalente and quadrivalent elements, Skrifter Norske Videnskaps–Akad. Oslo I. Mat.-Naturv. Kl., 8, 2, 1926.

Green, E. C. R., White, R. W., Diener, J. F. A., Powell, R., Holland, T. J. B., and Palin, R. M.: Activity–composition relations for the calculation of partial melting equilibria in metabasic rocks, J. Metamorph. Geol., 34, 845–869, 2016.

Gregurek, D., Abart, R., and Hoinkes, G.: Contrasting Eoalpine *P*–*T* evolutions in the southern Koralpe, Eastern Alps, Mineralogy, 60, 61–80, 1997.

Griffin, W.: GLITTER: data reduction software for laser ablation ICP-MS, in: Sylvester, P. (Ed.), Laser Ablation–ICP–MS in the Earth Sciences, Vol. 40, Mineralogical Association of Canada Short Course Series, 204–207 Appendix 2, 2008.

Haüy, R. J.: Traité de Minéralogie, Seconde édition, Tome deuxième, Bacheliere et Huzard, Paris, 1822.

Heede, H. U.: Isotopengeologische Untersuchungen an Gesteinen des ostalpinen Saualpenkristallins, Kärnten–Österreich, Münsterische Forschungen zur Geologie und Paläontologie, 81, 1–168, 1997.

Hermann, J., Spandler, C., Hack, A., and Korsakov, A. V.: Aqueous fluids and hydrous melts in high-pressure and ultra-high pressure rocks: Implications for element transfer in subduction zones, Lithos, 92, 399–417, 2006.

Hernández-Uribe, D., Hernández-Montenegro, J. D., Cone, K. A., and Palin, R. M.: Oceanic slab-top melting during subduction: Implications for trace-element recycling and adakite petrogenesis, Geology, 48, 216–220, 2020.

Holland, T. J. B. and Powell, R.: An improved and extended internally consistent thermodynamic dataset for phases of petrological interest, involving a new equation of state for solids, J. Metamorph. Geol., 29, 333–383, 2011.

Holland, T. J. B., Green, E. C., and Powell, R.: Melting of peridotites through to granites: a simple thermodynamic model in the system KNCFMASHTOCr, J. Petrol., 59, 881–900, 2018.

Holness, M. B. and Sawyer, E. W.: On the Pseudomorphing of Melt-filled Pores During the Crystallization of Migmatites, J. Petrol., 7, 1343–1363, 2008.

Janák, M., Froitzheim, N., and Yoshida, K.: Diamond in metasedimentary crustal rocks from Pohorje, Eastern Alps: a window to deep continental subduction, J. Metamorph. Geol., 33, 495–512, 2015.

Janoušek, V., Farrow, C. M., and Erban, V.: Interpretation of whole-rock geochemical data in igneous geochemistry: introducing Geochemical Data Toolkit (GCDkit), J. Petrol., 47, 1255–1259, 2006.

Jochum, K. P., Weis, U., Stoll, B., Kuzmin, D., Yang, Q., Raczek, I., Jacob, D. E., Stracke, A., Birbaum, K., Frick, D. A., Günther, D., and Enzweiler, J.: Determination of reference values for NIST SRM 610–617 glasses following ISO guidelines, Geostand. Geoanal. Res., 35, 397–429, 2011.

Kleinschmidt, G.: Die "Plankogelserie" in der südlichen Koralpe unter besonderer Berücksichtigung von Manganquarziten, Verh. Geol. B.-A, 1974, 351–362, 1974.

Kohlstedt, D. L. and Holtzman, B. K.: Shearing melt out of the Earth: An experimentalist's perspective on the influence of deformation on melt extraction, Annu. Rev. Earth Pl. Sc., 37, 561–593, 2009.

Kurz, W., Wölfler, A., Rabitsch, R., and Genser, J.: Polyphase movement on the Lavanttal fault zone (eastern Alps): reconciling the evidence from different geochronological indicators, Swiss J. Geosci., 104, 323–343, 2011.

Labrousse, L., Prouteau, G., and Ganzhorn, A.-C.: Continental exhumation triggered by partial melting at ultrahigh pressure, Geology, 39, 1171–1174, 2011.

Laurie, A. and Stevens, G.: Water-present eclogite melting to produce Earth's early felsic crust, Chem. Geol., 314, 83–95, 2012.

Leake, B. E., Woolley, A. R., Arps, C. E. S., Birch, W. D., Gilbert, M. C., Grice, J. D., Hawthorne, F. C., Kato, A., Kisch, H. J., Krivovichev, V. G., Linthout, K., Laird, J., Mandarino, J., Maresch, W. V., Nickel, E. H., Rock, N. M. S., Schumacher, J. C., Smith, D. C., Stephenson, N. C. N., Ungaretti, L., Whittacker, E. J. W., and Youzhi, G.: Nomenclature of amphiboles; Report of the Subcommittee on Amphiboles of the International Mineralogical Association Commission on New Minerals and Mineral Names, Europ. J. Mineral., 9, 623–651, 1997.

Manning, C. E.: Fluids of the lower crust: deep is different, Ann. Rev. Earth Pl. Sc., 46, 67–97, 2018.

Mibe, K., Kawamoto, T., Matsukage, K. N., Fei, Y., and Ono, S.: Slab melting versus slab dehydration in subduction-zone magmatism, P. Natl. Acad. Sci. USA, 108, 8177–8182, 2011.

Miladinova, I., Froitzheim, N., Nagel, T. J., Janak, M., Fonseca, R. O., Sprung, P., and Münker, C.: Constraining the process of intracontinental subduction in the Austroalpine Nappes: Implications from petrology and Lu-Hf geochronology of eclogites, J. Metamorph. Geol., 40, 423–456, 2022.

Miller, C.: Petrology of the type locality eclogites from the Koralpe and Saualpe (Eastern Alps), Austria, Schweiz. Miner. Petrog., 70, 287–300, 1990.

Miller, C. and Thöni, M.: Eo-Alpine eclogitisation of Permian MORB-type gabbros in the Koralpe (Eastern Alps, Austria): new geochronological, geochemical and petrological data, Chem. Geol., 137, 283–310, 1997.

Miller, C., Stosch, H., and Hoernes, S.: Geochemistry and origin of eclogites from the type locality Koralpe and Saualpe, Eastern Alps, Austria, Chem. Geol., 67, 103–118, 1988.

Miyazaki, T., Nakamura, D., Tamura, A., Svojtka, M., Arai, S., and Hirajima, T.: Evidence for partial melting of eclogite from the Moldanubian Zone of the Bohemian Massif, Czech Republic, J. Mineral. Petrol. Sci., 111, 405–419, 2016.

Pilger, N. and Schönenberg, R.: Geologie der Saualpe, Sonderband 1. Clausthaler Geologische Abhandlungen, Clausthal-Zellerfeld, 1975.

Powell, R. and Holland, T. J. B.: An internally consistent thermodynamic dataset with uncertainties and correlations: 3. Application, methods, worked examples and a computer program, J. Metamorph. Geol., 6, 173–204, 1988.

Powell, R., Guiraud, M., and White, R. W.: Truth and beauty in metamorphic phase equilibria: Conjugate variables and phase diagrams, Can. Mineral., 43, 21–33, 2005.

Putz, M., Stüwe, K., Jessel, M., and Calcagno, P.: Three-dimensional model and late stage warping of the Plattengneis Shear Zone in the Eastern Alps, Tectonophysics, 412, 87–103, 2006.

Rapp, J., Klemme, S., Butler, I., and Harley, S.: Extremely high solubility of rutile in chloride and fluoride-bearing metamorphic fluids: An experimental investigation, Geology, 38, 323–326, 2010.

Rebay, G., Powell, R., and Diener, J. F. A.: Calculated phase equilibria for a MORB composition in a P–T range, 450–650 °C and 18–28 kbar: the stability of eclogite, J. Metamorph. Geol., 28, 635–645, 2010.

Rocholl, A.: Major and trace element composition and homogeneity of microbeam reference material: Basalt glass USGS BCR-2G, Geostandard. Newslett., 22, 33–45, 1998.

Rogowitz, A. and Huet, B.: Evolution of fluid pathways during eclogitization and their impact on formation and deformation of eclogite: A microstructural and petrological investigation at the type locality (Koralpe, Eastern Alps, Austria), Tectonophysics, 819, 229079, https://doi.org/10.1016/j.tecto.2021.229079, 2021.

Rosenberg, C. L. and Handy, M. R.: Experimental deformation of partially melted granite revisited: implications for the continental crust, J. Metamorph. Geol., 23, 19–28, 2005.

Schmidt, M. W. and Poli, S.: Experimentally based water budgets for dehydrating slabs and consequences for arc magma generation, Earth Planet. Sc. Lett., 163, 361–379, 1998.

Schmidt, M. W. and Poli, S.: Treatise on geochemistry: The Crust,Vol. 4, chap. Devolatilization during subduction, 669–701, Elsevier, Amsterdam, 2014.

Schmidt, M. W., Vielzeuf, D., and Auzanneau, E.: Melting and dissolution of subducting crust at high pressures: the key role of white mica, Earth Planet. Sc. Lett., 228, 65–84, 2004.

Schorn, S.: Dehydration of metapelites during high-P metamorphism: The coupling between fluid sources and fluid sinks, J. Metamorph. Geol., 36, 369–391, 2018.

Schorn, S. and Diener, J.: Details of the gabbro-to-eclogite transition determined from microtextures and calculated chemical potential relationships, J. Metamorph. Geol., 35, 55–75, 2017.

Schorn, S. and Stüwe, K.: The Plankogel detachment of the Eastern Alps: petrological evidence for an orogen-scale extraction fault, J. Metamorph. Geol., 34, 147–166, 2016.

Schorn, S., Hartnady, M. I., Diener, J. F., Clark, C., and Harris, C.: H_2O-fluxed melting of eclogite during exhumation: an example from the eclogite type-locality, Eastern Alps (Austria), Lithos, 390, 106118, https://doi.org/10.1016/j.lithos.2021.106118, 2021.

Tafur, L. A. and Diener, J. F.: Mineral equilibrium constraints on the feasibility of diffusive H_2O-fluxed melting in the continental crust, J. Metamorph. Geol., 38, 719–742, 2020.

Thöni, M. and Jagoutz, E.: Some new aspects of dating eclogites in orogenic belts: Sm–Nd, Rb–Sr, and Pb–Pb isotopic results from the Austroalpine Saualpe and Koralpe type-locality (Carinthia/Styria, southeastern Austria), Geochim. Cosmochim. Ac., 56, 347–368, 1992.

Thöni, M. and Jagoutz, E.: Isotopic constraints for eo-Alpine high-P metamorphism in the Austroalpine nappes of the Eastern Alps: bearing on Alpine orogenesis, Schweiz. Miner. Petrog., 73, 177–189, 1993.

Thöni, M. and Miller, C.: Garnet Sm–Nd data from the Saualpe and the Koralpe (Eastern Alps, Austria): chronological and P–T constraints on the thermal and tectonic history, J. Metamorph. Geol., 14, 453–466, 1996.

Thöni, M. and Miller, C.: Andalusite formation in a fast exhuming high-P wedge: textural, microchemical, and Sm–Nd and Rb–Sr age constraints for a Cretaceous P–T–t path at Kienberg, Saualpe (Eastern Alps), Austrian J. Earth Sc., 103, 118–131, 2010.

Thöni, M., Miller, C., Blichert-Toft, J., Whitehouse, M., Konzett, J., and Zanetti, A.: Timing of high-pressure metamorphism and exhumation of the eclogite type-locality (Kupplerbrunn–Prickler Halt, Saualpe, south-eastern Austria): constraints from correlations of the Sm–Nd, Lu–Hf, U–Pb and Rb–Sr isotopic systems., J. Metamorph. Geol., 26, 561–581, 2008.

Turekian, K. K. and Wedepohl, K. H.: Distribution of the elements in some major units of the earth's crust, Geol. Soc. Am. Bull., 72, 175–192, 1961.

Turner, S. J. and Langmuir, C. H.: Sediment and ocean crust both melt at subduction zones, Earth Planet. Sc. Lett., 584, 117424, https://doi.org/10.1016/j.epsl.2022.117424, 2022.

Vinogradov, A. P.: The origin of the Earth's shells, Vestn. Alcad. Nauk SSSR 9, 16–29, NASA Tech. Transl. F-171, 1962.

Wang, L., Kusky, T. M., Polat, A., Wang, S., Jiang, X., Zong, K., Wang, J., Deng, H., and Fu, J.: Partial melting of deeply subducted eclogite from the Sulu orogen in China, Nat. Commun., 5, 5604, https://doi.org/10.1038/ncomms6604, 2014.

Wang, S.-J., Wang, L., Brown, M., Johnson, T. E., Piccoli, P. M., Feng, P., and Wang, Z.-L.: Petrogenesis of leucosome sheets in migmatitic UHP eclogites – Evolution from silicate-rich supercritical fluid to hydrous melt, Lithos, 105442, https://doi.org/10.1016/j.lithos.2020.105442, 2020.

Waters, D. J. and Whales, C. J.: Dehydration melting and the granulite transition in metapelites from southern Namaqualand, South Africa, Contrib. Mineral. Petrol., 88, 269–275, 1984.

Weissenbach, N., Pilger, N., and Schönenberg, R.: Geologische Karte der Saualpe (Kärnten). 1 : 25.000, Geologische Bundesanstalt, Wien, 2 Bl., 1978.

White, R. W., Powell, R., Holland, T. J. B., Johnson, T. E., and Green, E. C. R.: New mineral activity–composition relations for thermodynamic calculations in metapelitic systems, J. Metamorph. Geol., 32, 261–286, 2014a.

White, R. W., Powell, R., and Johnson, T. E.: The effect of Mn on mineral stability in metapelites revisited: new a–x relations for manganese-bearing minerals, J. Metamorph. Geol., 32, 809–828, 2014b.

Wohlers, A. and Baumgartner, L.: Melt infiltration into quartzite during partial melting in the Little Cottonwood Contact Aureole (UT, USA): implication for xenocryst formation, J. Metamorph. Geol., 31, 301–312, 2013.

Xia, B., Brown, M., Wang, L., Wang, S.-J., and Piccoli, P.: Phase equilibrium modeling of MT–UHP eclogite: A case study of coesite eclogite at Yangkou Bay, Sulu belt, Eastern China, J. Petrol., 59, 1253–1280, 2018.